

Determining the mid-plane conditions of circumstellar discs using gas and dust modelling: a study of HD 163296

Dominika M. Boneberg,¹★ Olja Panić,¹† Thomas J. Haworth,¹ Cathie J. Clarke¹ and Michiel Min^{2,3}

¹*Institute of Astronomy, Madingley Road, Cambridge CB3 0HA, UK*

²*SRON Netherlands Institute for Space Research, Sorbonnelaan 2, NL-3584 CA Utrecht, the Netherlands*

³*Astronomical Institute Anton Pannekoek, University of Amsterdam, Science Park 904, NL-1098 XH Amsterdam, the Netherlands*

Accepted 2016 May 27. Received 2016 May 27; in original form 2016 March 2

ABSTRACT

The mass of gas in protoplanetary discs is a quantity of great interest for assessing their planet formation potential. Disc gas masses are, however, traditionally inferred from measured dust masses by applying an assumed standard gas-to-dust ratio of $g/d = 100$. Furthermore, measuring gas masses based on CO observations has been hindered by the effects of CO freeze-out. Here we present a novel approach to study the mid-plane gas by combining C¹⁸O line modelling, CO snowline observations and the spectral energy distribution and selectively study the inner tens of au where freeze-out is not relevant. We apply the modelling technique to the disc around the Herbig Ae star HD 163296 with particular focus on the regions within the CO snowline radius, measured to be at 90 au in this disc. Our models yield the mass of C¹⁸O in this inner disc region of $M_{\text{C}^{18}\text{O}}(<90 \text{ au}) \sim 2 \times 10^{-8} M_{\odot}$. We find that most of our models yield a notably low $g/d < 20$, especially in the disc mid-plane ($g/d < 1$). Our only models with a more interstellar medium (ISM)-like g/d require C¹⁸O to be underabundant with respect to the ISM abundances and a significant depletion of sub-micron grains, which is not supported by scattered light observations. Our technique can be applied to a range of discs and opens up a possibility of measuring gas and dust masses in discs within the CO snowline location without making assumptions about the gas-to-dust ratio.

Key words: techniques: interferometric – protoplanetary discs – circumstellar matter – stars: pre-main sequence.

1 INTRODUCTION

Protoplanetary discs – discs of gas and dust that surround young pre-main-sequence stars – are the birthplaces of planets. With new observational facilities such as the Atacama Large Millimeter/submillimeter Array (ALMA) providing data of unprecedented resolution and sensitivity, we have the opportunity to study the disc structure and through it, the processes that lead to planet formation in more detail than ever before. However, interpretation of these observations is reliant upon comparison with the expected emission properties from numerical models of discs. Protoplanetary discs consist of gas and dust. In the interstellar medium (ISM), the mass ratio of these two components is canonically assumed to be $g/d = 100$ as has been inferred from observations (see e.g. Frerking, Langer & Wilson 1982; Lacy et al. 1994). Due to the lack of observational constraints thereof, this value is often also adopted

for discs. Panić et al. (2008) obtain a range between 25 and 100 for g/d from their modelling of the Herbig Ae/Be star HD 169142, depending on the dust opacity they assume, Meeus et al. (2010) narrowed down this range to ~ 22 –50. In 51 Oph, Thi et al. (2013) find a value of g/d consistent with 100, the same holds true for HD 141569 (Thi et al. 2014). The study by Williams & Best (2014) of several T Tauri stars yields g/d that are relatively low ($\lesssim 40$); the values they obtain for a few Herbig Ae/Be stars are also rather low, with the exception of HD 163296, where they obtain $g/d = 170$.

The gas governs the disc dynamics and motion of the dust, whereas dust provides the opacity to capture the stellar flux, re-radiate it and heat the disc. In order to understand the structure of discs, it is therefore crucial to study the spatial distribution and properties of both components (see e.g. Beckwith & Sargent 1987; Dutrey, Guilloteau & Simon 1994; Isella et al. 2007; Panić et al. 2008; Qi et al. 2011; Panić et al. 2014). Planets are believed to form in the disc mid-plane and thus understanding the disc conditions in these regions is particularly important for constraining models of planet formation (see e.g. Boley & Durisen 2010; Forgan & Rice 2013).

* E-mail: boneberg@ast.cam.ac.uk

† Royal Society Dorothy Hodgkin Fellow.

Many discs have bright emission in the millimetre (mm) continuum (e.g. Beckwith et al. 1990; Dutrey et al. 1996; Mannings & Sargent 1997; Andrews & Williams 2007; Andrews et al. 2009, 2010; Qi et al. 2011), tracing the dust in the disc. Due to the uncertainties associated with g/d and the dust grain properties, inferring the disc mass from continuum measurements is, however, only a rough approximation. Therefore, molecular emission lines are used alternatively or additionally and allow the inference of spatial and temperature structure. The most abundant molecule in discs is cold H_2 gas, however, this is difficult to observe due to the lack of a dipole moment and its low-transition probability. Thus, molecules such as ^{12}CO , ^{13}CO and C^{18}O and their respective transitions are employed instead.

Abundances of molecular tracers are influenced by the conditions in the disc: for example, CO can be photodissociated in the disc atmosphere or frozen out in the disc below a temperature of $T \approx 19$ K (Qi et al. 2011). Recently, it has been claimed that the exact value of the freeze-out temperature can vary from disc to disc (e.g. Qi et al. (2015) model the snowline at a temperature of 17 K in TW Hya and 25 K in HD 163296) and depends on the chemical history of the ice (Garrod & Pauly 2011). Moreover, the transitions of the CO emission lines become optically thick at different heights within the disc, depending on the abundance of the particular isotopologue (e.g. van Zadelhoff et al. 2001; Dartois, Dutrey & Guilloteau 2003; Miotello, Bruderer & van Dishoeck 2014) and thus optical depth effects compromise the ability to obtain disc masses from the more abundant species. C^{18}O is an important diagnostic of the unfrozen part of the disc mass, being much less abundant than other CO species ($[\text{C}^{18}\text{O}]/[\text{C}^{16}\text{O}] = 557 \pm 30$; Wilson 1999). Its transitions in the mm wavelength regime are mostly optically thin throughout the whole disc and thus provide an excellent probe of the disc mid-plane. This is evidently of great importance since most of the gas mass resides near the disc mid-plane and it is here that planets are expected to form. However, only a handful of observations of C^{18}O exist so far, including AB Aurigae (Semenov et al. 2005), HD 169142 (Panić et al. 2008), MWC480 (Akiyama et al. 2013), HD 142527 (Perez et al. 2015) and HD 163296 (Qi et al. 2011; Rosenfeld et al. 2013). There are also C^{18}O data available on several T Tauri stars studied by Williams & Best (2014). Furthermore, there exist observations of C^{18}O in TW Hya, V4046 Sgr, DM Tau, GG Tau and IM Lup (see Williams & Best 2014, and references therein).

The CO snowline radius is the location in the disc mid-plane at which CO condenses from the gas phase and freezes out on to dust grains. This radius can be observed as a steep decline in the C^{18}O density or by the presence of other molecular tracers such as N_2H^+ and DCO^+ (Qi et al. 2011; Mathews et al. 2013; Qi, Öberg & Wilner 2013b; Qi et al. 2015; Carney et al., in preparation). However, the formation path of DCO^+ is not fully understood and this molecule does not probe the disc mid-plane but the entire surface of the 19–21 K isotherms. Hence, Qi et al. (2015) find that DCO^+ is not a reliable tracer of the CO snowline location. They employ ALMA $\text{N}_2\text{H}^+\text{J} = 3-2$ observations instead that originate predominantly from the mid-plane and are therefore more reliable. The presence of gas-phase CO slows down the formation of N_2H^+ and accelerates its destruction. Thus, gas-phase N_2H^+ exists in regions where CO is depleted, so the N_2H^+ emission will be distributed in a ring whose inner radius marks the CO snowline location. Therefore, Qi et al. (2015) propose that observations of C^{18}O and N_2H^+ are very powerful as they directly probe the temperature of the disc mid-plane. This is important for calculations of the vertical hydrostatic equilibrium in discs which crucially depend on the conditions in

this disc region. However, the exact freeze-out temperature of CO is not known unambiguously, depends on the conditions of the environment and is assumed to be between ~ 17 K (Qi et al. 2013a, in TW Hya) and ~ 30 K (Jørgensen et al. 2015, in an embedded protostar). Also, the composition of the ice will influence the freeze-out temperature (~ 20 K for pure CO ice, ~ 30 K for mixed CO- H_2O ice; Collings et al. (2004)). In addition, the gas pressure can also have an impact on the freeze-out temperature (Fray & Schmitt 2009); however, Stammer et al. (in preparation) find that changes in the gas pressure in the disc mid-plane are not sufficient to shift the CO snowline radius by amounts which would cause an observable effect in our observations. Nevertheless, measurements of the snowline location are important as they give constraints on the mid-plane temperature profiles of discs.

Another important tool for studying protoplanetary discs is the spectral energy distribution (SED) that combines independent measurements in a range of wavelength regimes that trace different parts of the disc (see e.g. Boss & Yorke 1996; Dullemond 2002; Meijer et al. 2008, Panić et al., submitted, for studies of the influence of disc parameters on the resulting SED). As the dust content of the disc influences its opacity and thus determines how much stellar flux can be intercepted and re-radiated by the disc, the SED crucially depends on the properties and vertical distribution of dust. Thus, a combination of C^{18}O observations, additional data on the CO snowline radius and the SED provide a powerful combination of observables to model protoplanetary discs, combining independent measurements of both gas and dust.

In this paper, we model the disc around the $2.3 M_\odot$ (Qi et al. 2011) Herbig Ae star HD 163296, that is assumed to have an age of ~ 5 Myr (Natta et al. 2004). It is situated at a distance of about $d = 122$ pc (van den Ancker, de Winter & Tjin A Djie 1998) with a luminosity of $L = 37.7 L_\odot$ and an effective temperature of $T_{\text{eff}} = 9250$ K (Tilling et al. 2012). We list the observational properties of both the star and disc in Table 1. Interestingly, the outer radius of the disc as inferred from CO emission studies (Qi et al. 2011; de Gregorio-Monsalvo et al. 2013) and scattered light (Grady et al. 2000) is about double the value of the disc outer radius observed in the continuum (de Gregorio-Monsalvo et al. 2013). It is worth noting that HD 163296 is a relatively bright Herbig Ae star ($L_* = 37.7 L_\odot$; Tilling et al. 2012), thus, its disc is comparatively warm and its C^{18}O line emission strong. Furthermore, the disc is observed to have a gap in polarized light at $R_{\text{gap}} \sim 70$ au (Garufi et al. 2014).

Table 1. Observational stellar and disc properties of HD 163296 from: ¹Tilling et al. (2012), ²Qi et al. (2011), ³Natta et al. (2004), ⁴Grady et al. (2000), ⁵de Gregorio-Monsalvo et al. (2013), ⁶Guidi et al. (2016) and ⁷Qi et al. (2015). We use a Kurucz model for the star.

Stellar properties	Value
Spectral type ²	A1
Mass ² M_*	$2.3 M_\odot$
Effective temperature ¹ T_{eff}	9250 K
Luminosity ¹ L_*	$37.7 L_\odot$
Distance ² d	122 pc
Age ³ t	~ 5 Myr
Disc parameters	Value
Outer radius (scattered light) ⁴ $R_{\text{out, sc}}$	~ 500 au
Outer radius (continuum, $850 \mu\text{m}$) ^{5,6} $R_{\text{out, cont}}$	$\sim 240\text{--}290$ au
Outer radius (CO observations) ⁵ $R_{\text{out, CO}}$	~ 550 au
CO snowline radius ⁷ R_{sl}	90 au

Table 2. Summary of the available ALMA observations (molecular lines in Bands 6 and 7).

Molecular lines	Synthesized beam(arcsec)	rms (σ)(Jy beam ⁻¹)
C ¹⁸ O J = 2–1 (SV)	0.73 × 0.58	2 × 10 ⁻²
¹² CO J = 2–1 (SV)	0.68 × 0.55	5 × 10 ⁻²
¹³ CO J = 2–1 (SV)	0.72 × 0.57	3 × 10 ⁻²
¹² CO J = 3–2 (SV)	0.65 × 0.42	5 × 10 ⁻²

Its molecular lines (mostly CO) and continuum have been studied in detail in the mm and sub-mm (Mannings & Sargent 1997; Natta et al. 2004; Isella et al. 2007; Qi et al. 2011) and recently also with ALMA (de Gregorio-Monsalvo et al. 2013; Rosenfeld et al. 2013; Mathews et al. 2013; Flaherty et al. 2015; Qi et al. 2015; Guidi et al. 2016).

Rosenfeld et al. (2013), de Gregorio-Monsalvo et al. (2013) and Qi et al. (2015) employed ALMA data for modelling of the disc of HD 163296 but we are the first to use the C¹⁸O J = 2–1 data to model disc parameters. Rosenfeld et al. (2013) focused mainly on modelling CO and ¹³CO, whereas de Gregorio-Monsalvo et al. (2013) analysed the Band 7 data (¹²CO J = 3–2 and continuum) and Guidi et al. (2016) were most interested in the dust properties and hence the continuum observations. Qi et al. (2015) also studied the C¹⁸O emission, but they were mostly interested in analysing the snowline location and comparing the C¹⁸O and N₂H⁺ emission. In addition, Flaherty et al. (2015) used the available C¹⁸O data, but focused on the turbulence in the disc. We describe the relevant ALMA observations in the next section and stress that we base our modelling on the available ALMA C¹⁸O data as a crucial ingredient.

Qi et al. (2011) had inferred a snowline radius $R_{\text{sl}} \sim 155$ au from ¹³CO observations which was consistently also derived by Mathews et al. (2013) from DCO⁺ observations. However, more recent studies by Qi et al. (2015) find a snowline radius $R_{\text{sl}} \sim 90$ au from both N₂H⁺ and C¹⁸O ALMA observations.

We do not aim to provide one best-fitting model for the disc around HD 163296, but rather want to emphasize the degeneracies in the parameters of the modelling process and propose a way to overcome them. Our main goal is to investigate the mid-plane gas temperature and density in this disc using a novel modelling approach. In Section 2, we summarize and discuss the observations. In Section 3, we describe in detail our modelling process and all the steps involved. In Section 4, we specify the models we obtain, their implications and potential degeneracies and also discuss their properties. We summarize our findings and conclusions in Section 5.

2 ALMA OBSERVATIONS

2.1 Description of observations

Science verification data of HD 163296 were taken by ALMA in Band 6 and 7 (Rosenfeld et al. 2013). The ALMA observations are provided as 3D fits cubes with two spatial and one spectral axis (velocity/frequency) on the ALMA Portal.¹ There is calibrated and cleaned data with a resolution of ~ 0.7 arcsec (~ 85 au at $d = 122$ pc) available for ¹²CO J = 2–1, ¹³CO J = 2–1 and C¹⁸O J = 2–1 (all Band 6), as well as for ¹²CO J = 3–2 (Band 7). We list the corresponding rms noise values and beam sizes in Table 2. We use the Common Astronomy Software Applications, CASA software package version

4.4.0 (McMullin et al. 2007), to analyse the respective transitions. Amongst the transitions listed above, the C¹⁸O J = 2–1 is relatively unexplored and the one on which our work focusses. We employ the already self-calibrated and cleaned Science Verification data provided on the ALMA Portal.

C¹⁸O J = 2–1 observations (Band 6) of HD 163296 (RA= 17^h56^m21^s.281, Dec. = –21°57′22″.36; J2000) were taken with 24 ALMA antennas (12 m) in 2012, on June 9 and 23 and July 7 with baselines spanning 20–400 m and a total on-source time of 84 min (Rosenfeld et al. 2013). For a detailed summary of the spectral windows and calibrations, see Rosenfeld et al. (2013). The beam size of the reduced and cleaned C¹⁸O data is 0.73 arcsec × 0.58 arcsec, the spectral resolution is 0.33 km s⁻¹ (~ 0.24 MHz) with 150 channels, ranging from 219.571 to 219.534 GHz, where the rest frequency of the transition is 219.56 GHz. We plot the integrated emission and intensity-weighted velocity maps of C¹⁸O J = 2–1 in Fig. 1 and describe them in more detail in the next section. We find an integrated intensity of C¹⁸O J = 2–1 of 6.2 ± 0.4 Jy km s⁻¹, which is consistent with the values obtained by Qi et al. (2011, 2015) and Rosenfeld et al. (2013).

2.2 Spatial structure of the emission

We plot the frequency-integrated intensity maps and intensity-weighted velocity maps for both transitions of ¹²CO, as well as C¹⁸O and ¹³CO in Fig. 1.² We will focus in more detail on C¹⁸O in this paper, but show all of these maps here as we explore the disc geometry also by using these other molecular species. Additionally, we present the continuum map of Band 6. From the extent of the disc in the panels of Fig. 1, it is clear that the molecular species and the continuum trace different parts of the disc. The CO isotopes of different abundances trace down to varying depths in the disc, due to their different opacities.

Using the CASA software package, we can determine the position angle (PA) of the disc from C¹⁸O observations (image deconvolved from beam), which we find to be PA = (132.8 ± 3.4) °. This is in agreement with what other studies have found from CO and continuum observations (Qi et al. 2011; Rosenfeld et al. 2013). Fitting a 2D Gaussian to the spatial profile of the emission with CASA allows us to determine the inclination of the disc for the different tracers shown in Fig. 1 (where $i = 0$ corresponds to the disc being face-on). From the C¹⁸O emission, we obtain an inclination of $i = (47.9 \pm 1.6)$ °, which is comparable to the inclination of $i = 44$ ° used by Qi et al. (2011). For the other molecular species, we performed the same analysis and obtained the values given in Table 3. The value we find for the PA from the ¹²CO J = 3–2 is comparable with the one from de Gregorio-Monsalvo et al. (2013), however, we find a larger inclination in comparison to their value (38 °). The PA and inclination for the continuum emission in Band 6 and 7 are slightly lower than the values obtained from the gas lines. However, gas and dust can trace regions of the disc with different outer radii. It might thus be possible that the inner regions of the disc have a different inclination. Also, the calculations of the PA and inclination from the CO emission might be influenced by the fact that the line emission seems to have a slightly boxy shape in comparison to the ellipses in the continuum (see Fig. 1). For our models, we will adapt a

² As already pointed out in Rosenfeld et al. (2013), the SV data of ¹²CO J = 3–2 have a velocity offset and is falsely centred around a velocity of 6.99 km s⁻¹ instead of the systemic velocity of 5.8 km s⁻¹. We have taken this offset into account for the respective velocity map.

¹ <https://almascience.nrao.edu/alma-data/science-verification/overview>

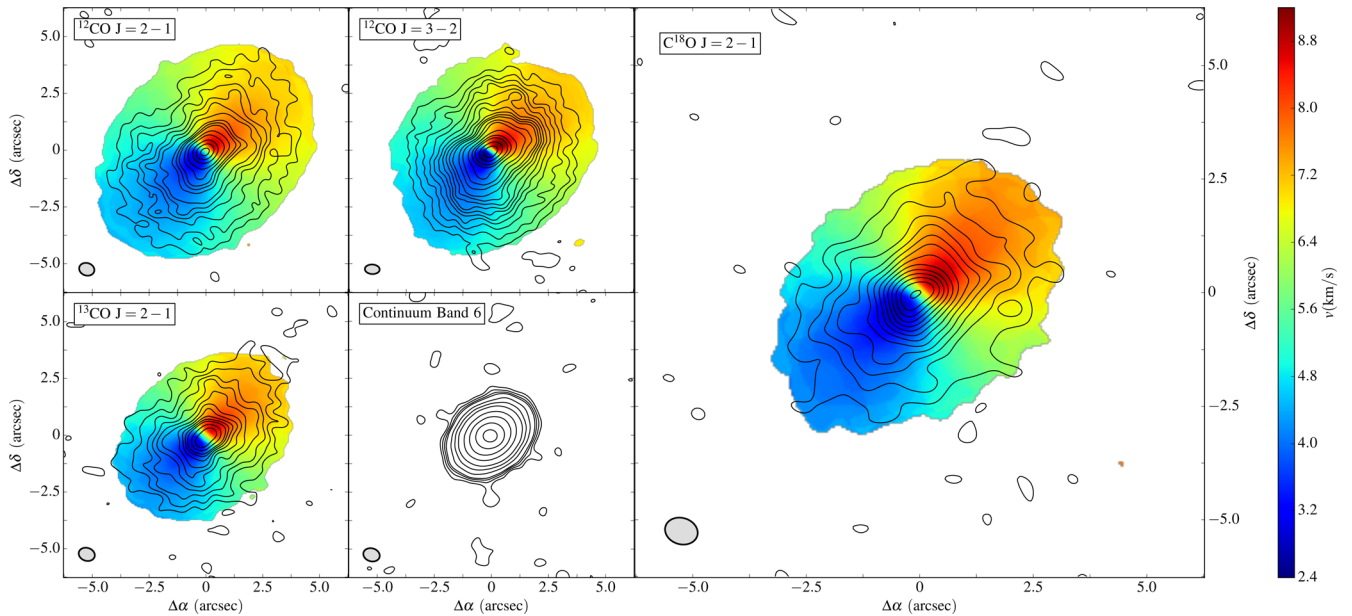


Figure 1. Integrated line emission (contours) and intensity-weighted velocity (colour) maps of $^{12}\text{CO J} = 2-1$, $^{12}\text{CO J} = 3-2$, $^{13}\text{CO J} = 2-1$, $\text{C}^{18}\text{O J} = 2-1$ and continuum map of Band 6. The contours are levels of $(2, 4, 6, 8, \dots) \times \sigma$ noise. The innermost contour has the following levels: $\sim 100 \times \sigma$ ($^{12}\text{CO J} = 2-1$), $\sim 100 \times \sigma$ ($^{12}\text{CO J} = 3-2$), $\sim 28 \times \sigma$ ($^{13}\text{CO J} = 2-1$), $\sim 52 \times \sigma$ ($\text{C}^{18}\text{O J} = 2-1$) and $\sim 796 \times \sigma$ (continuum). The velocity maps discard the data at a level $\lesssim 5 \times \sigma$ noise. The respective σ are given in Table 2. The synthesized beam is plotted in the bottom-left corner of each panel.

Table 3. Molecular species and continuum emission in Bands 6 and 7 and the respective PAs and inclinations ($i = 0$ is face-on) including their errors obtained from their integrated intensity maps with CASA.

Molecular species and continuum	PA($^\circ$)	Inclination i ($^\circ$)
$^{12}\text{CO J} = 2-1$	138.0 ± 2.0	48.4 ± 2.3
$^{13}\text{CO J} = 2-1$	133.7 ± 2.7	46.5 ± 1.5
$\text{C}^{18}\text{O J} = 2-1$	132.8 ± 3.4	47.9 ± 1.6
Continuum Band 6	131.4 ± 2.1	42.8 ± 0.1
$^{12}\text{CO J} = 3-2$	140.4 ± 1.9	44.7 ± 0.9
Continuum Band 7	130.3 ± 1.1	43.1 ± 0.1

PA = 132° and an inclination of $i = 48^\circ$, which is widely in agreement with the values obtained from the fits.

3 MODELLING

3.1 Physical models

3.1.1 Modelling the 2D structure of the disc

Our modelling process is two-fold: we first model the 2D temperature and density structure of the disc using the radiative transfer code MCMAX (Min et al. 2009), ensuring that our models match the observed SED and CO snowline radius. We then take these models as an input to the TORUS code (Harries 2000) which performs molecular line radiative transfer; we use synthetic C^{18}O line profiles to further narrow down the range of viable models. We primarily aim to determine the magnitude of various parameter degeneracies, rather than to calculate a single best-fitting model.

MCMAX: We use the 3D radiative transfer code MCMAX, which self-consistently calculates a 2D temperature and density structure of the model with Monte Carlo radiative transfer (Min et al. 2009).

The input parameters are the radial variation of the gas and dust surface density (fixed as being proportional to r^{-p} where p is in the range 1–1.2), the total dust mass (and grain size distribution, a_{\min} and a_{\max}), the gas-to-dust ratio, g/d and the turbulent mixing parameter α_{turb} . We then use MCMAX to iteratively compute the temperature, and from it the resulting vertical profile of the gas density. This profile satisfies hydrostatic equilibrium normal to the disc plane in the gas and thermal equilibrium in the dust (assuming the gas and dust temperatures are equal). The vertical profile of the dust (including dust settling) is obtained by solving a diffusion equation for each dust particle size bin and normalizing the vertically averaged value of the gas-to-dust ratio at each radius to the input value of g/d .

The solution is self-consistent in the sense that the dust and gas profiles are not independently prescribed: the dust affects the hydrostatic equilibrium of the gas by setting the temperature, whereas the gas profile affects the degree of dust settling and hence, through variation of the amount of starlight intercepted, the temperature profile of the dust. For each iteration on the thermal structure of the dust, photon packages emitted from the star (which is the source of heating) are followed through the disc. They are (re-)absorbed, re-emitted and scattered off the dust grains multiple times. This is the primary source of heating for the dense regions of the disc which are of interest for the C^{18}O emission. This treatment would probably not be suitable for the inner few au of the mid-plane, where viscous heating usually dominates. The mass accretion rate of HD 163296 is derived to be within the range $(0.8\text{--}4.5) \times 10^{-7} M_{\odot} \text{ yr}^{-1}$ (Garcia Lopez et al. 2015) from Br- γ observations, so depending on its value, viscous heating could potentially be important in the very inner disc regions (\sim few au). Given that we are interested in mid-plane regions further out, we do not take this effect into account.

Based on the stellar properties and the disc structure, a 2D temperature profile for the disc is thus obtained in thermal equilibrium.

MCMAX then iterates the gas density profile so as to obtain vertical hydrostatic equilibrium given by

$$\frac{dP}{dz} = -\rho(r, z) \frac{dF_{\text{grav},z}}{dz}, \quad (1)$$

where P is the pressure, ρ the gas density and $F_{\text{grav},z}$ the gravitational potential in z -direction. Dust settling is included in MCMAX by solving a diffusion equation for each grain size as detailed in Mulders & Dominik (2012). We explore values of the turbulent mixing parameter in MCMAX between $\alpha_{\text{turb}} = 10^{-4}$ and 10^{-2} , which is a frequently adopted range of values for protoplanetary discs (Mulders & Dominik 2012). The value of α_{turb} is hard to derive from observations and is assumed to be in the range of ~ 0.5 – 10^{-4} (Isella, Carpenter & Sargent 2009). For HD 163296, Flaherty et al. (2015) find a value of $\alpha_{\text{turb}} \leq 9 \times 10^{-4}$ in the upper layers of the outer disc. In general, this parameter determines the strength of the mixing of the gas and dust components for a given gas-to-dust mass ratio g/d . Furthermore, α_{turb} is, in general, lower at low altitudes in the disc (Simon et al. 2015). Increasing the turbulent mixing parameter leads to a stronger mixing of gas and dust, enabling more small dust grains to be stirred up to the disc atmosphere where they can intercept more stellar light. All MCMAX models with the same $M_{\text{gas}} \times \alpha_{\text{turb}} = \text{const.}$ yield exactly the same SED and CO snowline location. This can be understood following the discussion in Youdin & Lithwick (2007): for a regime where the dimensionless stopping time $\tau_s = \Omega_k \times t_{\text{stop}}$ (with the Keplerian orbital frequency Ω_k and the particle stopping time t_{stop}) is smaller than the dimensionless eddy turnover time $\tau_e = \Omega_k \times t_{\text{eddy}}$ (with t_{eddy} the eddy turnover time), i.e. $\tau_s < \tau_e < 1$, the scaleheight of particles H_p divided by the scaleheight of the gas H_{gas} is given by

$$\frac{H_p}{H_{\text{gas}}} \propto \sqrt{\frac{\alpha_{\text{turb}}}{\tau_s}}. \quad (2)$$

Given that $\tau_s \propto t_{\text{stop}}$, equation (2) can be modified in the Epstein regime, where $t_{\text{stop}} \propto \rho_{\text{grain}} \times s \cdot c_s^{-1} \times \rho_{\text{gas}}^{-1}$ (with ρ_{grain} being the

internal grain density, s the grain size, c_s the sound speed and ρ_{gas} the gas density), hence

$$\frac{H_p}{H_{\text{gas}}} \propto \sqrt{\alpha_{\text{turb}} \times \rho_{\text{gas}}}. \quad (3)$$

This implies that $H_p \propto H_{\text{gas}}^{-1}$ and thus, the temperature and dust structure are kept invariant when $\rho_{\text{gas}} \times \alpha_{\text{turb}}$ (and thus $g/d \times \alpha_{\text{turb}}$) are kept constant. Consequently, models that fulfil this criterion have exactly the same SED, temperature structure and dust density structure. For our modelling process, we first run models with a turbulent mixing strength of $\alpha_{\text{turb}} = 10^{-4}$ and fit these to the observed SED, but then run additional calculations for these models, exploring larger values of α_{turb} (10^{-3} and 10^{-2}) while decreasing the gas masses in these models by factors of 10 and 100, accordingly, to keep the temperature structure and SED the same. The new models are named A–E/10 and A–E/100, respectively. We will call all models that have the same dust parameters and constant $\alpha_{\text{turb}} \times g/d$ models of the same series.

We perform the above iterations using 5×10^7 photon packages and 350 grid cells in the azimuthal direction and 400 in radial direction. We have checked for convergence in the Monte Carlo radiative transfer calculation by increasing the number of photon packets. However, since the Poisson noise scales with the square root of the number of photon packets, this is inefficient. We therefore stack the average density and temperature structure over the last few well-converged iterations of the MCMAX calculation to reduce both the noise and computational expense.

Modelling the SED: In general, each of our models is unique in some aspect (see distinctive feature in last column of Table 4 where we list the individual model parameters). We make an extreme assumption for one of the varied parameters at a time and then search for the SED fit in order to obtain the wide range of properties without the necessity of doing a complete parameter space exploration. We generate a range of models by varying the following parameters: the mass of dust M_{dust} , the minimum dust grain size a_{min} , maximum grain size a_{max} and the gas-to-dust ratio g/d (alone, as well as in combination with the turbulent mixing strength α_{turb}). We assume

Table 4. Parameters of our 15 models that fit the observed SED: M_{dust} , M_{gas} , g/d , a_{min} , a_{max} and $T_{\text{mid-plane}}$ at the location of the CO snowline radius $R_{\text{sl}} = 90$ au. We also give the power-law exponent p of the surface density profile $\Sigma \propto r^{-p}$. We list as well the turbulent mixing strength α_{turb} and the mm opacity κ_{mm} of the dust grains that MCMAX is using. The respective distinctive characteristics of the models are given in the last column. Models (A–E)/10 and (A–E)/100 have the same dust properties as models A–E, but their g/d (and thus their M_{gas}) are divided by factors of 10 (100) and their α_{turb} multiplied by 10 (100) in comparison with models A–E. The models given in boldface are the models that also match the observed C¹⁸O line profiles as we will discuss in the next section.

Model	$M_{\text{dust}}(M_{\odot})$	$M_{\text{gas}}(M_{\odot})$	g/d	$a_{\text{min}}(\mu\text{m})$	$a_{\text{max}}(\text{mm})$	$T(90 \text{ au})(\text{K})$	$-p$	α_{turb}	$\kappa_{\text{mm}}(\text{cm}^2 \text{g}_{\text{dust}}^{-1})$	Distinctive features
A	3.0×10^{-3}	3.0×10^{-1}	100	0.8	35	25.0	1.0	10^{-4}	~ 0.9	high M_{dust} and M_{gas}
B	8.0×10^{-4}	1.4×10^{-1}	180	0.8	0.4	22.5	1.0	10^{-4}	~ 4.0	high g/d
C	8.0×10^{-4}	8.0×10^{-2}	100	0.5	1.1	22.0	1.0	10^{-4}	~ 3.6	intermediate-sized dust
D	9.5×10^{-4}	1.0×10^{-2}	10.5	0.02	1.4	23.5	1.0	10^{-4}	~ 3.3	low g/d, pristine dust
E	1.3×10^{-3}	1.2×10^{-2}	9.2	0.05	1.4	20.0	1.2	10^{-4}	~ 3.3	steeper $\Sigma(r)$-profile
A/10	3.0×10^{-3}	3.0×10^{-2}	10	0.8	35	25.0	1.0	10^{-3}	~ 0.9	–
B/10	8.0×10^{-4}	1.4×10^{-2}	18	0.8	0.4	22.5	1.0	10^{-3}	~ 4.0	–
C/10	8.0×10^{-4}	8.0×10^{-3}	10	0.5	1.1	22.0	1.0	10^{-3}	~ 3.6	–
D/10	9.5×10^{-4}	1.0×10^{-3}	1.05	0.02	1.4	23.5	1.0	10^{-3}	~ 3.3	–
E/10	1.3×10^{-3}	1.2×10^{-3}	0.92	0.05	1.4	20.0	1.2	10^{-3}	~ 3.3	–
A/100	3.0×10^{-3}	3.0×10^{-3}	1	0.8	35	25.0	1.0	10^{-2}	~ 0.9	–
B/100	8.0×10^{-4}	1.4×10^{-3}	1.8	0.8	0.4	22.5	1.0	10^{-2}	~ 4.0	–
C/100	8.0×10^{-4}	8.0×10^{-4}	1	0.5	1.1	22.0	1.0	10^{-2}	~ 3.6	–
D/100	9.5×10^{-4}	1.0×10^{-4}	0.11	0.02	1.4	23.5	1.0	10^{-2}	~ 3.3	–
E/100	1.3×10^{-3}	1.2×10^{-4}	0.09	0.05	1.4	20.0	1.2	10^{-2}	~ 3.3	–

in every case that the grains follow a power-law size distribution of $n(a) \propto a^{-k}$, where a is the grain size. The value for ISM grains, that is often also adopted for discs, is $k = 3.5$ (see e.g. Mathis, Rumpl & Nordsieck 1977; Clayton et al. 2003), which results in most of the dust mass being in the largest grains, while the opacity is provided by the smallest dust.

We choose to vary these five disc parameters in our modelling as they have the biggest effect on the SED (Meijer et al. 2008, Panić et al., submitted). We explore a range of M_{dust} going from the lowest possible value that can still reproduce the mm flux in the SED as we will describe in Section 4.1 up to ~ 0.1 per cent of the stellar mass. We initially vary g/d between 10 and 200 to explore an extreme range around the ISM value (while fixing $\alpha_{\text{turb}} = 10^{-4}$). Once we find a combination of α_{turb} and g/d that provide a match, we then explore other combinations of these two parameters, taking into account the above described degeneracy of $\alpha_{\text{turb}} \times g/d$. The grains sizes we assume range from pristine dust (sub-micron-sized) to mm or even cm-sized grains in some cases.

The stellar properties that we use for all of our models are listed in Table 1 and are kept fixed. We use a Kurucz model for the star, which sets the stellar emission. Given the values for the outer radius as inferred from CO observations, we use a value of $R_{\text{out}} = 540$ au for our models. We then investigate how our parameter choices affect the resulting SED and the predicted radius of the CO snowline. Rather than finding the single model that provides the best fit to these observables, we instead identify a range of models that provide an acceptable fit and then, as detailed in the following section, further isolate the models that additionally match the line fluxes in C^{18}O .

3.1.2 Modelling of the C^{18}O line emission

The models we obtain from the analysis described above are then taken as an input density and temperature structure for the next modelling step. We use the radiation transport and hydrodynamics code TORUS to perform molecular line transfer calculations in this paper (see e.g. Harries 2000; Rundle et al. 2010; Haworth & Harries 2012). TORUS is capable of molecular statistical equilibrium calculations and the production of synthetic data cubes (e.g. for one specific molecular transition). Full details of the main molecular line transfer algorithm are given by Rundle et al. (2010); we summarize key and new features below.

We map the gas density and temperature distributions from the 2D spherical MCMAX calculations on to the 2D cylindrical TORUS grid using a bi-linear interpolation in r and θ . We assume that the gas and dust are thermally coupled (allowing us to map the dust temperature directly on to the gas). Although TORUS is capable of non-local thermodynamic equilibrium (LTE) molecular line transport, for application to these disc models, the densities are sufficiently high and the assumption of LTE produces identical results as non-LTE calculations.³ Therefore, the level populations can be characterized as a Boltzmann distribution, that is as a simple function of temperature

$$\frac{n_i}{\sum_i n_i} = \frac{g_i \exp\left(\frac{-E_i}{kT_{\text{gas}}}\right)}{z(T_{\text{gas}})}, \quad (4)$$

³ The assumption of LTE is prudent in the mid-plane for mm lines (in which we are interested as they preferentially probe the disc mid-plane), but might not be sufficient for the infrared (IR) lines.

where g_i is the statistical weight and $z(T_{\text{gas}}) = \sum_i g_i \exp\left(\frac{-E_i}{kT_{\text{gas}}}\right)$ the partition function. With the level populations computed, synthetic data cubes are calculated using ray tracing (Rundle et al. 2010). TORUS allows for flexible choice of observer viewing angle and spectral/spatial resolution. We implement a model for freeze-out, whereby the C^{18}O abundance drops to a negligible value if the temperature is below the freeze-out temperature (which is $T_{\text{mid-plane}}(90 \text{ au})$ of the respective model. We list these temperatures in Table 4. To evaluate the effect of photodissociation of CO by the stellar irradiation, we implement a simple criterion, qualitatively similar to that of Williams & Best (2014). We assume that for a CO particle column density of $N_{\text{CO}} \approx 10^{18} \text{ cm}^{-2}$ in the line of sight from the star, all CO molecules will be photodissociated. This is only a crude estimate, however, it allows us to check how much of the total gas mass is affected and to gauge the impact on our model. The value we adopt implies a larger role for photodissociation than that employed by Williams & Best (2014) (who use $N_{\text{H}_2} \approx 1.3 \times 10^{21} \text{ cm}^{-2}$, corresponding to $N_{\text{CO}} \approx 1.3 \times 10^{17} \text{ cm}^{-2}$ for $f_{\text{CO}} \approx 10^{-4}$). We also explore the effect of adopting even larger column density thresholds of $N_{\text{CO}} \approx 10^{19} \text{ cm}^{-2}$ and $\approx 10^{20} \text{ cm}^{-2}$, the latter of which certainly exaggerates the effect of photodissociation.

Turbulence affects the line emission to a much lesser extent than the temperature and density do, and these effects are only marginally discerned in observations of higher signal to noise lines, such as those of ^{12}CO and at a high spectral resolution. Our assumption of turbulent velocity v_{turb} therefore does not affect our fit to the C^{18}O data. The maximum turbulent line broadening possible is set by the sound speed in the outer mid-plane

$$c_s = \sqrt{\frac{k_B T_{\text{mid}}(r_{\text{out}})}{\mu m_{\text{H}}}}, \quad (5)$$

where k_B is the Boltzmann constant, T_{mid} the mid-plane temperature, μ the mean molecular weight and m_{H} the atomic mass of hydrogen. Following Simon et al. (2015), we employ a value of $0.01\text{--}0.1c_s$, suitable in the outer disc mid-plane, for the turbulent line broadening in TORUS. Given that the temperature in the outer mid-plane is approximately $T \approx 8$ K, we find

$$v_{\text{turb}} = (0.01\text{--}0.1) \times c_s(8 \text{ K}) = (0.0017\text{--}0.017) \text{ km s}^{-1}, \quad (6)$$

where $\mu = 2.37$. The recent study by Flaherty et al. (2015) also suggests that turbulence is relatively weak in the HD 163296 disc ($v_{\text{turb}} < 0.03c_s$ in the upper layers of the outer disc), supporting our low value of v_{turb} . Changing v_{turb} by a factor of 10 in our models does not alter the fit to the observations of C^{18}O , as the data quality does not allow us to probe v_{turb} sufficiently well. Also, since C^{18}O is mainly optically thin, turbulent broadening will cause slight smearing of the line profile, but will not affect the line flux. This would be different if we were studying a more optically thick transition like for example CO $J = 3\text{--}2$ (see e.g. Flaherty et al. 2015). The turbulent line broadening is related to the turbulent mixing parameter α_{turb} by

$$v_{\text{turb}} \sim \sqrt{\alpha_{\text{turb}}} c_s. \quad (7)$$

The above means that $\alpha_{\text{turb}} = 10^{-4}\text{--}10^{-2}$ is implicit in this calculation. Flaherty et al. (2015) find $\alpha_{\text{turb}} < 9.6 \times 10^{-4}$ from their modelling of HD 163296. We explore this range of values of α_{turb} in Section 4.1, but we hereby stress that for a wide range of α_{turb} and corresponding values of v_{turb} our fit to the line emission remains unaffected.

Another aspect to take into account is that the fractional abundance (by number density) of $C^{18}O$ is uncertain. This abundance is given by

$$f_{C^{18}O} = \frac{[CO]}{[H_2]} \cdot \frac{[C^{18}O]}{[CO]}, \quad (8)$$

where we assume that $[C^{18}O]/[CO] = [^{18}O]/[^{16}O]$. Therefore, uncertainty in the isotopic ratio of ^{16}O to ^{18}O as well as in the fractional abundance of CO have to be taken into account. The abundance of CO is altered due to freeze-out (mid-plane) and photodissociation (surface) (see e.g. Panić et al. 2008; Miotello et al. 2014). The ISM abundance of $[CO]/[H_2] \sim 10^{-4}$ (Aikawa & Nomura 2006) is usually also assumed for discs. However, it is important to note that there is a significant scatter around this value: Lacy et al. (1994) find a maximum value of the fractional abundance of ^{12}CO of 9.1×10^{-4} , whereas Frerking et al. (1982) obtain a value of $\sim 8.5 \times 10^{-5}$ in ρ Oph and Taurus. Given the isotopic ratio of $[^{16}O]/[^{18}O]$ and its errors (557 ± 30 ; Wilson 1999), the resulting $C^{18}O$ fractional abundance we employ is in a range between

$$1.4 \times 10^{-7} < \frac{[C^{18}O]}{[H_2]} < 1.7 \times 10^{-6}. \quad (9)$$

The maximum effect of this uncertainty on the line emission is achieved in the optically thin case, where the line emission scales linearly with the abundance. We take this fully into account when presenting the results of our calculations of the $C^{18}O$ line emission. $C^{18}O J = 2-1$ is excited by molecular collisions within the disc. The shape of its line is thus dependent on the temperature and density structure of the disc and on the $C^{18}O$ mass available.

Using the CASA software package, we further process the data cubes to obtain synthetic ALMA observations that take into account filtering and instrumental and thermal noise effects. These can then be directly compared with or fitted to the observational $C^{18}O$ data (e.g. molecular line profiles).

4 RESULTS AND DISCUSSION

4.1 Results of the SED modelling

Initial mass estimate: We have explored in total over 100 models varying M_{dust} , a_{min} , a_{max} and g/d (alone, and in combination with α_{turb}) and have found 15 models that fit the observed SED, the details of the models are given in Table 4.

In order to fit our model to the observed SED, we start from an initial estimate of the minimum dust mass, which determines the overall SED shape. If the resulting fluxes in the SED are too high compared to the observations, we decrease the dust mass. If the mm-wavelength fluxes are too high at shorter wavelengths, but not in the mm, we reduce the g/d ratio. We then make further improvements on the fit by varying the minimum and maximum grain size, taking into account the effects of the individual disc parameters on the SED. For model series B–E, we have based our initial dust mass estimate on the following considerations: for optically thin emission, the dust mass is given by

$$M_{\text{dust}} = \frac{S_{\lambda} d^2}{\kappa_{\lambda} B_{\lambda}(T)}, \quad (10)$$

where S_{λ} is the flux at a certain wavelength, d the distance of the source in pc and κ_{λ} the opacity at wavelength λ . B_{λ} is the Planck function depending on the temperature, given by

$$B_{\lambda} = \frac{2hc^2}{\lambda^5} \left[\exp\left(\frac{hc}{\lambda k_B T}\right) - 1 \right]^{-1}, \quad (11)$$

where h is the Planck constant and k_B the Boltzmann constant. For a distance of $d \approx 120$ pc (van den Ancker et al. 1998), temperature $T \approx 20$ K and at a wavelength of $\lambda \approx 0.85$ mm, we find a flux of $S_{\lambda} \approx 2.1$ Jy (Guidi et al. 2016). We thus estimate a minimum dust mass of $M_{\text{dust, min}} \sim 8 \times 10^{-4} M_{\odot}$. Here, the opacity we assume is given in Draine (2006), who shows that at $\lambda \approx 1$ mm, dust grains of size $a \approx 1$ mm are most efficient emitters with $\kappa_{\lambda} \approx 4 \text{ cm}^2 \text{ g}_{\text{dust}}^{-1}$, as they contain most of the mass (they are, however, not the most efficient emitters per unit mass). Table 4 shows that this grain size is comparable to the maximum grain size a_{max} of model series C–E. These models therefore represent the case when the bulk of the mass is in ~ 1 mm-sized grains and M_{dust} is low. For a grain size of 0.4 mm as in model series B, κ_{λ} from Draine (2006) is a little lower, leading to a slightly higher minimum dust mass than in model series D to reproduce the same SED. Note, however, that we used the above calculation only to get an initial value for M_{dust} , employing standardized values for the opacity. The mm opacities κ_{mm} we are using with MCMAX are given in Table 4, they depend on the dust grain size, thus they vary from model to model and differ slightly from the values given in Draine (2006), which are for a material of specific chemical composition and properties assumed to be similar to ISM dust. However, the mm opacities only influence the exact location of the mm point in the SED.

Our models: The SEDs of all our models are given in Fig. 2. As discussed above, all models of a given model series have the same SED due to the degeneracy of α_{turb} and g/d . We include a zoom-in of the far-infrared (FIR) and mm region of the SED as this is the wavelength regime that is most crucial for our analysis. All our models match the observed SED in this wavelength range very well, therefore the different models are hardly distinguishable there. We do not try to fit the observed SED at wavelengths $\lambda \gtrsim 2$ mm because emission in this regime can be dominated by free-free emission (Wright et al. 2015; Guidi et al. 2016), which is not included in our calculations. Note that the only models which can reproduce the $\lambda > 2$ mm observations by thermal emission – and no free-free emission at all – are the models of series A, D and E, where series A needs large grains (35 mm) and all three of them a high dust mass. Furthermore, the models do not match the near-infrared (NIR) excess at $\lambda < 10 \mu\text{m}$ very well, but this is sensitive to the exact dust grain composition and geometry of the very inner disc (inner few au; Meijer et al. 2008). Including a puffed-up inner disc rim, which could potentially cast a shadow on to the disc surface, might be expected to provide a better fit to the NIR SED. However Acke et al. (2009) find that this would only influence the NIR regime of the SED (not the FIR or mm). Therefore, a puffed-up inner rim would not improve the fit over a substantial wavelength range. The NIR fit does not alter our results for the dust mass, which is calculated using the longer wavelength component of the SED. Furthermore, adjusting the scaleheight in the inner disc would violate the self-consistency of our models. For simplicity, we therefore do not include a model for a puffed up inner rim at this stage.

Description of model series (A, B, C, D, E): We will first discuss the general characteristics of each of these models. We find that model A has a relatively high M_{dust} and M_{gas} (of the order of 10 per cent of the stellar mass $M_{*} = 2.3 M_{\odot}$). This will in general produce relatively high fluxes, so in order to compensate for the high masses, its grains have to be quite evolved. This will ensure that not too many small grains are situated in the disc atmosphere, where they could intercept stellar irradiation and thus boost the fluxes of the SED. Models B and C have the same M_{dust} , but due to their different g/d

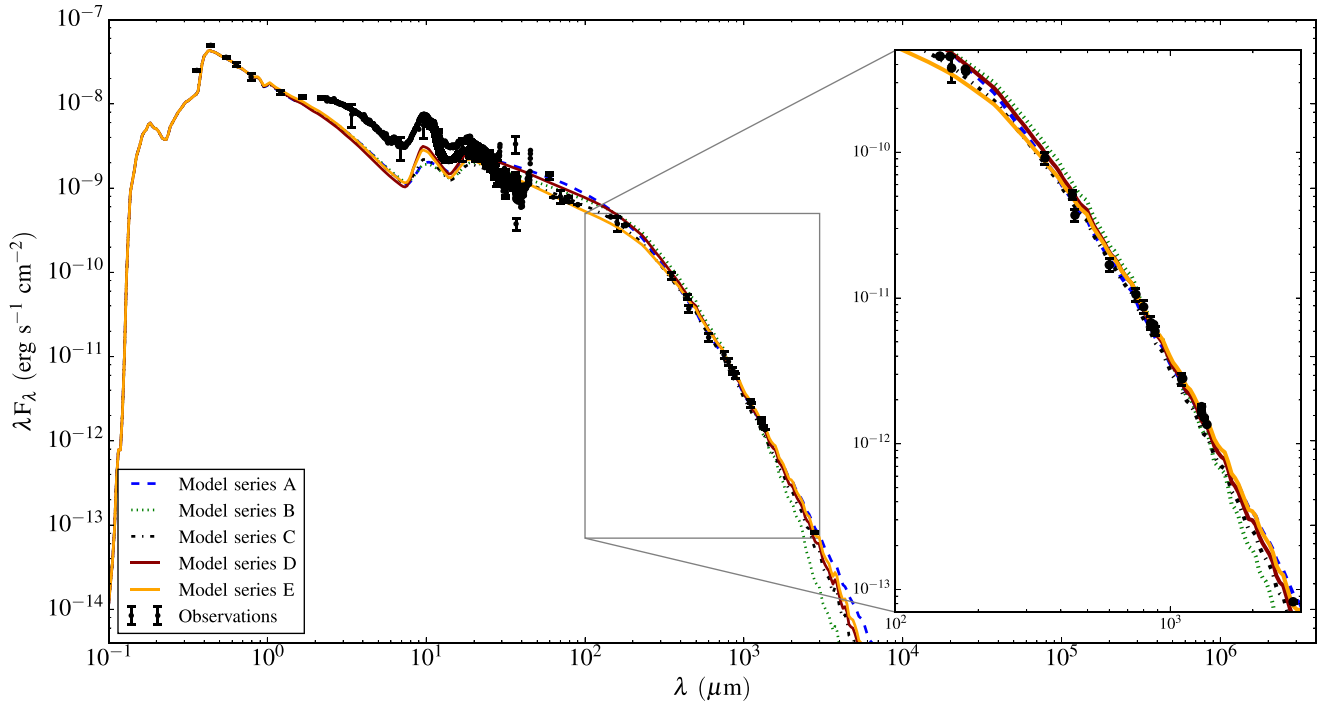


Figure 2. SEDs of our best-fitting models (parameters can be found in Table 4). Due to the degeneracy of α_{turb} and g/d , the SEDs within each model series are exactly the same (see the text). The observations are plotted as black circles including the respective error bars. The observational data are taken from Berrilli et al. (1992), Mannings & Sargent (1997), Bouwman et al. (2000), Isella et al. (2007), Qi et al. (2011), Tilling et al. (2012), Mendigutía et al. (2012), de Gregorio-Monsalvo et al. (2013) and the *Spitzer* c2d legacy survey.

ratios, their M_{gas} values differ by about a factor of 2. In order for them to give the same SEDs, model B with the higher g/d has to have different grain sizes from model C: its minimum grain size is a little larger than for model C, while its maximum grain size is about a factor of 3 smaller. The distinctive feature of model B is its high g/d ratio which we compensate for by making its minimum grain size bigger than in model C. Therefore – as described for model A – the fluxes in the SED are reduced. Models D and E have a much lower gas mass than the other models we found, but they all have the same SED. This is caused by these two models being the only ones with very small grains. These are coupled to the gas, dragged to higher layers and thus intercept more stellar flux. In general, models A–C have relatively large grain sizes (which probably corresponds to a more evolved state), otherwise the SEDs would produce too high values in the FIR. Model E is similar to model D, but employs a different radial dependence of the surface density: for models series A–D, we assumed $\Sigma \propto r^{-1}$, for model series E, we take a slightly steeper profile of $r^{-1.2}$, although still well within the range of observationally measured values for protoplanetary discs (Andrews et al. 2010). Model series E yields a lower mid-plane temperature at the location of the CO snowline radius than the other models, as we will discuss shortly.

We have calculated the optical depth of the continuum emission for our models (using the surface density and mm opacity), which yields that the mm continuum emission for all our models is optically thin, except for model series E, where it becomes optically thick within the inner ~ 10 au. This enables us to obtain a reliable estimate of the dust mass in the disc. We would like to highlight that some of our models reach the maximum mm opacity (as obtained by Draine 2006) and are indicative of the minimum $M_{\text{dust}} \sim 8 \times 10^{-4} M_{\odot}$ as derived earlier in this section. Much lower κ_{mm} are of

course possible if a big fraction of the mass is hidden in pebbles and larger bodies, which do not contribute to the mm flux. In such cases, M_{dust} in our models is just indicative of the mass of the mm dust and thus a much higher total mass of solids can be achieved. However, such models would not differ in the SED.

Variations of model series (A–E/10, A–E/100): Models A–E have a turbulent mixing strength of $\alpha_{\text{turb}} = 10^{-4}$, but as described above, we run additional calculations for these models, exploring larger values of α_{turb} (10^{-3} and 10^{-2}) while decreasing the gas masses in these models by factors of 10 and 100. We leave all the remaining parameters of models A–E unchanged, as listed in Table 4. Indeed, we find that we can match the observational constraints given by the SED and mid-plane temperature requirements by all our models A–E, by changing the M_{gas} and adjusting the α_{turb} accordingly, to keep $M_{\text{gas}} \times \alpha_{\text{turb}}$ (and therefore the dust diffusion solution, resulting temperature structures and the SEDs within each model series) constant. In general, all models A–E/10 and A–E/100 yield low to very low g/d ratios by construction. In order to compensate for the lower gas masses, higher levels of turbulent mixing are needed to transport the dust grains to higher altitudes in the disc where they can absorb the stellar light and give the same SED. Given that the dust grain properties within a certain series are exactly the same, our above description of the distinctive features of models A–E holds true for (A–E)/10 and (A–E)/100, respectively.

In general, a surprising result of our modelling is that we can match both the SED and CO snowline radius, by making very different assumptions on the basic parameters, such as dust grain size and gas mass. Higher emission can for example be caused by a higher dust or gas mass, but also by smaller dust grains present in the disc. Some of these parameter degeneracies are also discussed in

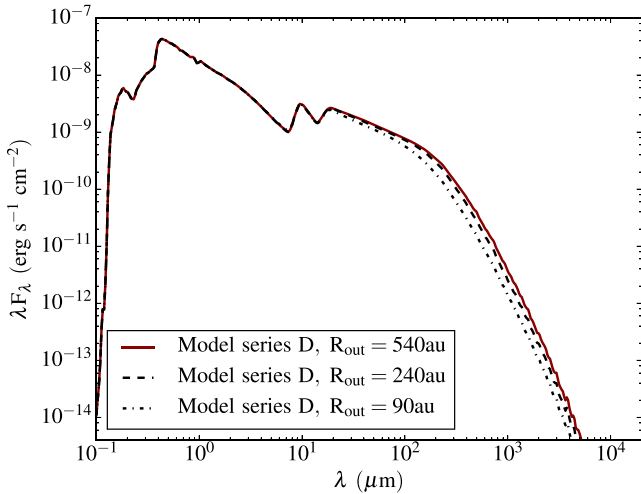


Figure 3. SED of the whole disc $R < 540$ au (red solid line), from within $R < R_{\text{dust},850\mu\text{m}} = 240$ au (black dashed line) and from $R < R_{\text{sl}} = 90$ au (black dash-dotted line).

Meijer et al. (2008), Woitke et al. (2016) and Panić et al. (submitted). It is therefore important to note that SED modelling alone does not provide unambiguous physical models of the disc structure, but is highly degenerate.

4.2 Disc regions determining the SED

Fitting observed SEDs in general is most suited for the inner disc regions, since dust grains in the outer disc regions do not intercept sufficient stellar light to contribute substantially to the SED. We have checked that the SEDs as obtained from the whole discs ($R = 540$ au) of our 15 models (as shown in Fig. 2), are only marginally changed when taking the emission from within 240 au. This is plotted in Fig. 3 for model series D, we find the same behaviour for the other models. Thus, the fact that our model discs are described by a single power-law surface density distribution out to 540 au (whereas the observed dust distribution extends only to ~ 240 au) will not have a significant effect on our SED fits. We will later focus on the gas budget of the disc within the CO snowline ($R_{\text{sl}} = 90$ au) and note that, in our models, this region contributes around 40–50 per cent of the flux at sub-mm wavelengths. We also overplot the SED for the emission from within the snowline radius in Fig. 3.

4.3 Models matching the CO snowline location

As an additional constraint we have to make sure that our MCMAX models are consistent with the observed CO snowline location. Therefore, we analyse the mid-plane temperature profile $T_{\text{mid-plane}}(r)$ for all our models that match the observed SED, which we plot in Fig. 4. As mentioned above, models of the same series have the same temperature structure. We find that all of them have mid-plane temperatures between ~ 20 and 25 K at the observed snowline radius of $R_{\text{sl}} \approx 90$ au (Qi et al. 2015). These are well within the range of values generally assumed and observed for the freeze-out temperature of CO: The freeze-out temperature can vary between ~ 20 and ~ 30 K depending on whether CO is binding to pure CO ice or a mixture with water ice (Collings et al. 2004), which is, in turn, also dependent on the chemical history of the ice (Garrod & Pauly 2011). In general, the CO freeze-out temperature is not known unambiguously and might vary from system to system (Hersant et al. 2009; Qi

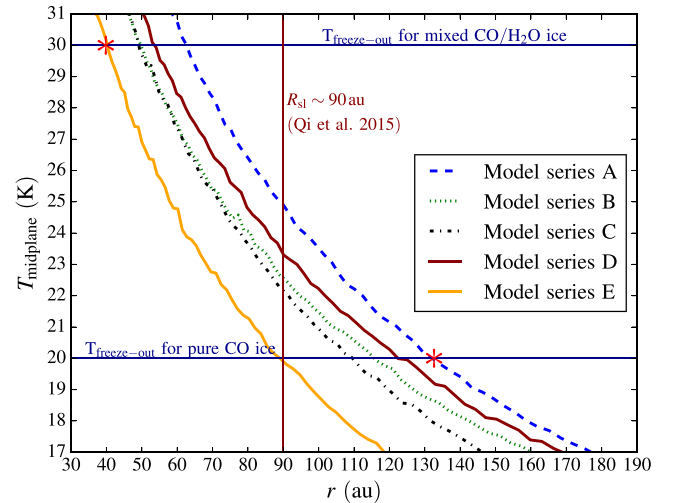


Figure 4. Mid-plane temperature as a function of radius for our 15 disc models that match the observed SED. Models from the same series have exactly the same mid-plane temperature structure (see Section 3.1.1). In dark red (vertical), we plot the observed snowline radius ≈ 90 au (Qi et al. 2015). The upper and lower limits of the freeze-out temperature (~ 20 – 30 K) as found by e.g. Collings et al. (2004) are plotted as horizontal lines. The red asterisks indicate where the snowline location could be between ~ 40 and 135 au due to a plausible range of freeze-out temperatures of 20 – 30 K if the snowline location was not known unambiguously from observations.

et al. 2015): Qi et al. (2013a) found a freeze-out temperature of CO of 17 K from their modelling of TW Hya, whereas Jørgensen et al. (2015) obtain temperatures of about 30 K in their study of embedded protostars. Qi et al. (2011) assume a freeze-out temperature for CO of $T \approx 19$ K (pure CO ice) for HD 163296. However, in Qi et al. (2015), they perform a new analysis with higher resolution observational data and use a temperature in the mid-plane at R_{sl} of $T \approx 25$ K (mixed CO/H₂O ice). Thus, all our models have temperatures in the disc mid-plane at the location of the snowline that are well within the plausible range. Our exploration of self-consistent models confirms that all the freeze-out temperatures assumed in these previous literature references fall within the plausible range of temperatures for HD 163296. If the freeze-out temperature of CO was known unambiguously, this would, in combination with an observationally determined CO snowline location, be a powerful model discriminant and we might be able to exclude models based on this constraint. Since, however, it is unclear what exactly the relevant freeze-out temperature is, we find that all the models can match the observed snowline location of 90 au. This weak model discrimination also means that it is impossible to predict the CO snowline radius from SED model fitting alone or even from fitting the molecular line emission together with the SED (Qi et al. 2011): given the uncertainty in the sublimation temperature of CO, our viable SED fits imply predicted radii in the range ~ 40 – 135 au as denoted by the red asterisks in Fig. 4. In general, we find that the location of the CO snowline radius does not further discriminate between models in comparison to the criterion given by the SED; however, it sets the radial location inwards of which no freeze-out is taking place in our models, and which is therefore important for the interpretation of the C¹⁸O emission. It is important to note that an SED fit does not determine the CO snowline location and that, vice versa, a CO snowline observation does not discriminate amongst possible SED models.

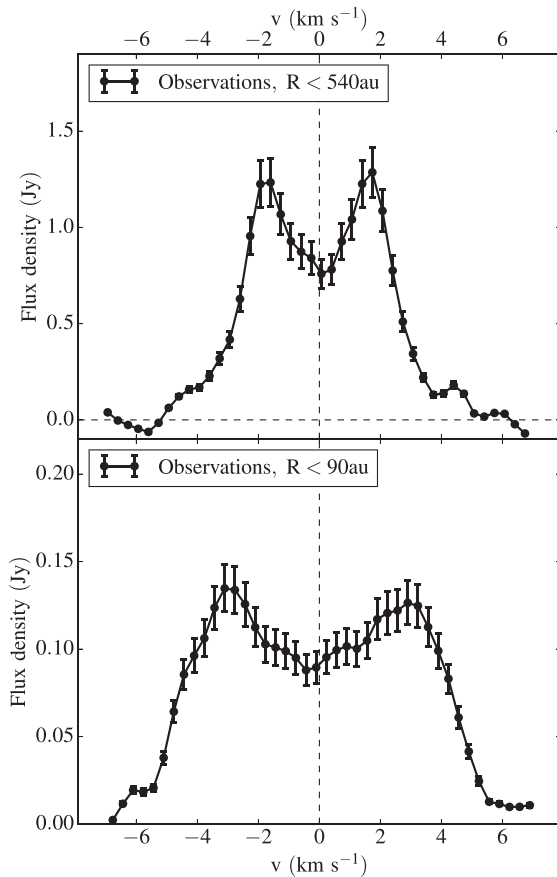


Figure 5. $\text{C}^{18}\text{O } J=2-1$ line profile (ALMA observations) using the emission from the whole disc (upper panel) and from within the 90 au snowline radius. The error bars represent a 10 percent flux calibration uncertainty (Guidi et al. 2016). We centred the spectra on 0 km s^{-1} . The systemic velocity is $v_{\text{sys}}=5.8 \text{ km s}^{-1}$.

We conclude that all our 15 models match the SED and CO snowline location within the uncertainties in the freeze-out temperature. The SED modelling is especially powerful for the inner ~ 240 au and describes the disc structure inside the CO snowline location well.

4.4 $\text{C}^{18}\text{O } J=2-1$ emission

4.4.1 C^{18}O line profiles

As discussed in Section 3.1.2, we use the density and temperature structures of our MCMAX models to calculate the C^{18}O line emission with TORUS. The aim of our work is to interpret the observed $\text{C}^{18}\text{O } J=2-1$ line profile, especially from the inner disc regions, in the context of a physically consistent model that matches other relevant observations (R_{sl} , SED). We show the $\text{C}^{18}\text{O } J=2-1$ line profile as observed by ALMA in Fig. 5, both taking the emission from the whole disc and from within the 90 au snowline radius. These are very different, especially in the peaks of the spectrum, as these are dominated by the emission from the outer disc regions. Our goal is to model the disc regions with $R < 90$ au (the snowline location), as these are independent of the details of freeze-out in the outer disc.

Uncertainty in abundance of C^{18}O : As mentioned previously, the fractional abundance of C^{18}O has a large uncertainty and is observed

(in star-forming clouds) to be in a range between 1.4×10^{-7} and 1.7×10^{-6} (see Section 3.1.2), thus spanning an order of magnitude. From matching the observed $\text{C}^{18}\text{O } J=2-1$ line profile with our models, we can unambiguously calculate the mass of C^{18}O in the disc. However, when converting this mass to a mass of H_2 , we will have to take into account this range of C^{18}O abundance.

Matching the observed C^{18}O line profile, we find that – taking into account the range of plausible abundances – only five of our models can fulfil this criterion, namely (A–C)/10, D and E. We will thus focus on these models in the further discussion.

Another aspect to take into account is that the abundance of C^{18}O in comparison to H_2 can be altered due to freeze-out in the disc mid-plane, as already discussed in the previous section. We have implemented this effect in TORUS by setting the abundance of C^{18}O to a negligible value when the disc temperature drops below the freeze-out temperature. For the individual models, we use the mid-plane temperature of the respective model at the observed snowline radius as given in Fig. 4. The fraction of the C^{18}O mass removed by freeze-out in the respective models is given in Table 5. We find that this effect is stronger for models (A–C)/10 than for models D and E, because the former have slightly higher gas masses and bigger grains, thus a higher fraction of the mass will be concentrated in the cooler disc mid-plane regions and thus subject to freeze-out. However, the exact impact of freeze-out on the line profile will depend on the details of the vertical temperature profile and thus on the location of the CO ice surface.

The second most relevant source of CO-removal from the gas-phase is photodissociation (Visser, van Dishoeck & Black 2009; Miotello, Bruderer & van Dishoeck 2014). As described in Section 3.1.2, we have taken this into account in our modelling. We do this by setting the C^{18}O abundance to a negligible value for a threshold column density of gas calculated from the star in different azimuthal directions covering the entire disc height. These threshold column densities vary from $N_{\text{CO}}=10^{18} \text{ cm}^{-2}$, 10^{19} cm^{-2} and 10^{20} cm^{-2} (corresponding to $10^{22} \text{ H}_2 \text{ cm}^{-2}$, $10^{23} \text{ H}_2 \text{ cm}^{-2}$ and $10^{24} \text{ H}_2 \text{ cm}^{-2}$, respectively, assuming $f_{\text{CO}} \sim 10^{-4}$). We find that overall only a small fraction of C^{18}O is photodissociated within the 90 au snowline location in our models. For the first threshold, the fraction of the CO gas mass photodissociated is ~ 0.1 per cent in all our models, for $N_{\text{CO}} = 10^{19} \text{ cm}^{-2}$, it is ~ 1 per cent and even for the extreme case, only ~ 3 per cent is photodissociated within the snowline radius. We calculate the C^{18}O line emission for $R < 90$ au after removing CO from the photodissociated layer, in the three explored cases ($N_{\text{CO}}=10^{18} \text{ cm}^{-2}$, 10^{19} cm^{-2} and 10^{20} cm^{-2}). This is presented for the example of model D in Fig. 6. Given that, in our analysis, we mostly focus on the regions within the 90 au snowline radius that are not subject to freeze-out and not strongly affected by photodissociation, our models are not dependent on the exact details of these processes.

The inner disc regions ($R < 90$ au): For 5 out of our 15 initial models, we can match the observed $\text{C}^{18}\text{O } J=2-1$ line profile within the range of plausible C^{18}O abundances between 1.4×10^{-7} and 1.7×10^{-6} (equation 9). We show the C^{18}O spectra arising from the regions inside the 90 au snowline radius in these models in the left-hand panels of Fig. 7. We will call these five models (A–C)/10, D and E ‘fiducial’ models in the further discussion. We obtain these from the synthetic and ALMA data cubes using the CASA software in the following way: we calculate the emission from an elliptical region, centred on the centre of the disc using a PA = 132° and a ratio of minor to major axis $\frac{b}{a} = \cos i$, where $i = 48^\circ$.

Table 5. Freeze-out temperatures (mid-plane temperatures at 90 au) and fractions of the CO mass removed in the various model series due to freeze-out.

Model series	A	B	C	D	E
$T_{\text{freeze-out}}$ (90 au) (K)	25.0	22.5	22.0	23.5	20.0
	~48 per cent	~45 per cent	~40 per cent	~27 per cent	~23 per cent

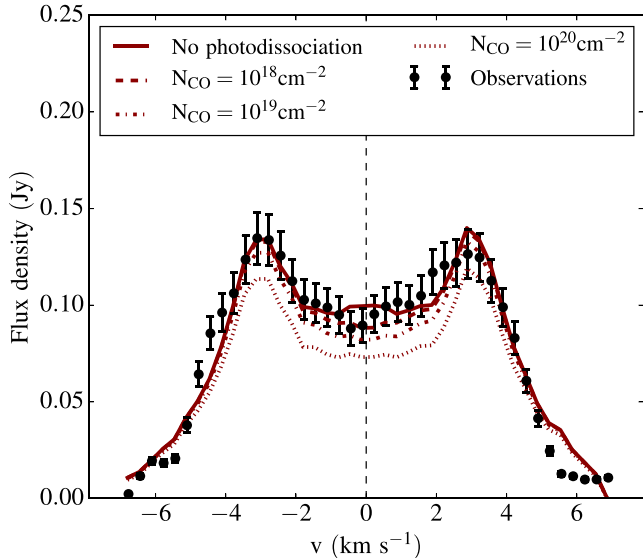


Figure 6. C^{18}O flux density for model D (from regions with $R < R_{\text{sl}} = 90$ au) employing different column density thresholds for photodissociation: no photodissociation (solid), $N_{\text{CO}} = 10^{18} \text{ cm}^{-2}$ (dashed), 10^{19} cm^{-2} (dash-dotted) and 10^{20} cm^{-2} (dotted). Even in the most extreme case, only ~ 3 per cent of the CO mass is affected. For reference, we also plot the observed line profile for this disc region, given by the black points with error bars (10 per cent flux calibration uncertainty). We find a very similar behaviour for the other models and thus do not show the respective plot here.

These values of PA and inclination are the ones we obtained in the analysis of the observations (see Section 2). All of them match the observations well within the error bars (given by the ~ 10 per cent flux calibration uncertainty of the ALMA observations; Guidi et al. 2016). The fractional abundances of C^{18}O of these models can be found in Table 6. Given these abundances and the gas masses in the respective models, we can calculate the mass of C^{18}O within the snowline radius, as the $\text{C}^{18}\text{O } J = 2-1$ transition is mainly optically thin throughout the whole disc. We have calculated the optical depth of the $\text{C}^{18}\text{O } J = 2-1$ transition and found that it is indeed optically thin throughout the whole line profile and at all radii for all our models that match the observations. Although the models are optically thin, this would not have been a necessary precondition for our modelling process as the radiative transfer calculation self-consistently accounts of optical depth effects. However, the low optical depths emphasizes how essential C^{18}O is as a tracer for the disc mid-plane. That implies that we can unambiguously calculate the $M_{\text{C}^{18}\text{O}}$ within 90 au which should be approximately the same for all our models. The values we obtain are listed in Table 6 and are in a range of

$$M_{\text{C}^{18}\text{O}}(R < 90 \text{ au}) \approx 2-3 \times 10^{-8} M_{\odot}. \quad (12)$$

The values that Qi et al. (2011) obtain for these inner disc regions are comparable to ours. In the right-hand panels of Fig. 7, we plot the emission from a bigger disc region, namely from within the

outer dust radius $R_{\text{dust}} \approx 240$ au. Our models still closely match the wings of the spectrum and thus the emission from the inner disc regions. However, one can see that our models slightly overpredict the emission from the outer disc regions (i.e. in the peaks of the spectrum) there. The height of the peaks depends crucially on the exact vertical temperature structure of the models as freeze-out will reduce the C^{18}O emission, especially in the outer disc regions. However, we do not attempt to match these disc regions, but focus on the innermost 90 au.

Models with minimum and maximum g/d : So far, we have only explored the five models from our initial Table 4 that also match the C^{18}O line profile. However, it is interesting to look into the extreme cases, i.e. models with minimum and maximum plausible C^{18}O abundance (and thus maximum and minimum g/d and M_{gas}), while still matching the observed C^{18}O and thus the C^{18}O masses within 90 au we just calculated. We give the properties of the extreme models in Table 7. It is important to note that models D_{max} and E_{max} can be excluded as their α_{turb} is lower than the minimum of 10^{-4} we assume. Models D and E both have this minimum value; therefore for model series D and E, the highest possible values of g/d and therefore M_{gas} within 90 au are the ones given in Table 6. The highest possible values of g/d for models that match the observed C^{18}O line profiles are 82 and 71 (for models B_{max} and C_{max} , respectively); the lowest value is 2 (model A_{min}). We take these three cases into account for the further discussion as they are the extreme ends of the g/d range we obtain.

Modelling the entire disc: Finally, for completeness, we compare the synthetic line profile for the whole disc with observations in Fig. 8. We see that our models overpredict the emission from the outer disc regions, i.e. the emission in the peaks of the spectrum. However, as we mentioned earlier, the SED does not provide information about the structure of the outermost disc regions. Also, we know that there are radial differences in the structure of the outer disc and the inner 240 au and we therefore limit our attention to the disc inner regions in this paper. It might be interesting to combine our modelling approach for the inner disc regions with high-resolution imaging of multiple isotopologues in the outer disc regions (see e.g. Qi et al. 2011; de Gregorio-Monsalvo et al. 2013).

4.4.2 Physical properties of our models

Gas mass within the snowline radius: The match to the observed C^{18}O spectrum within the CO snowline which we find for our five models unambiguously constrains the mass of C^{18}O in this disc region. In equation (12), we gave this mass within the snowline radius. We thus calculate the mass of H_2 in this disc region from $M_{\text{C}^{18}\text{O}}(90 \text{ au})$ by taking into account the abundance of C^{18}O given in Table 6 and the mass ratio of these molecules $m_{\text{C}^{18}\text{O}}/m_{\text{H}_2} \approx 14$. We find that the mass of H_2 within the snowline radius is in a range of $M_{\text{gas}}(R < 90 \text{ au}) \approx (1.3-5.0) \times 10^{-3} M_{\odot}$.

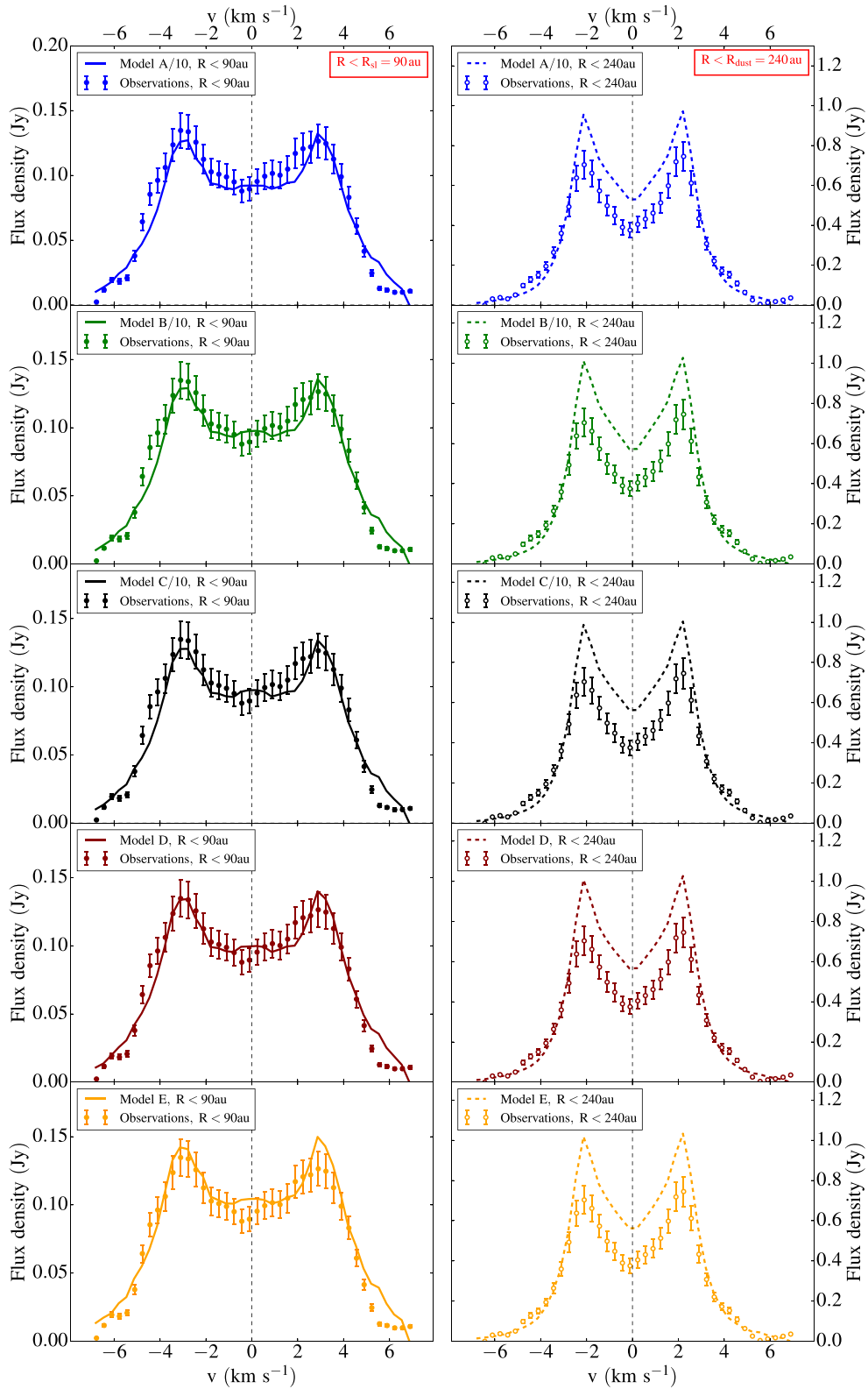


Figure 7. C^{18}O $J = 2-1$ line profiles for our five models: we show the emission from within the CO snowline radius (90 au) as well as from a disc region with $R < 240$ au (this corresponds to the outer disc radius as obtained from mm continuum observations). The line profiles from our models are given by the lines (solid for $R = 90$ au, dashed for $R = 240$ au), the spectra of the observations by the respective dots. The error bars reflect the 10 per cent flux calibration uncertainty of the observations. All models of the same series that have abundances in the range of C^{18}O abundances we consider will have the same flux densities because the C^{18}O masses and temperature structures are the same for each of these model series. The profiles were centred around 0 km s^{-1} (the systemic velocity is $v_{\text{sys}} = 5.8 \text{ km s}^{-1}$).

Table 6. Properties of our five best-fitting (fiducial) models: fractional abundance of $C^{18}O$ as obtained by matching the observed line profile within the 90 au snowline radius, the mass of $C^{18}O$ within this radius, the H_2 mass within the snowline radius, the average g/d within 90 au and α_{visc} for the respective cases.

Property	A/10	B/10	C/10	D	E
$f_{C^{18}O}$	2.7×10^{-7}	6.4×10^{-7}	1.0×10^{-6}	6.6×10^{-7}	6.8×10^{-7}
$M_{C^{18}O}(R < 90 \text{ au}) (M_{\odot})$	1.9×10^{-8}	2.1×10^{-8}	1.9×10^{-8}	1.6×10^{-8}	2.7×10^{-8}
$M_{\text{gas}}(R < 90 \text{ au}) (M_{\odot})$	5.0×10^{-3}	2.3×10^{-3}	1.3×10^{-3}	1.7×10^{-3}	2.9×10^{-3}
$M_{\text{dust}}(R < 90 \text{ au}) (M_{\odot})$	5.0×10^{-4}	1.3×10^{-4}	1.3×10^{-4}	1.6×10^{-4}	3.1×10^{-4}
g/d	10	18	10	10.5	9.2
$\alpha_{\text{visc}}(R < 90 \text{ au})$	0.2	0.4	0.7	0.5	0.3

Table 7. ‘Extreme’ cases of model series A–E: models with the highest possible g/d (and thus $M_{\text{gas}}(R < 90 \text{ au})$) are denoted by the ‘max’, the corresponding lowest models by ‘min’. We give the following parameters: fractional abundance of $C^{18}O$ as obtained by matching the observed line profile within the 90 au snowline radius, the mass of $C^{18}O$ within this radius, the H_2 mass within the snowline radius, the average g/d within 90 au, α_{turb} and α_{visc} for the respective cases. Models D_{max} and E_{max} can be excluded as their α_{turb} is outside the range we assume.

Model	$f_{C^{18}O}$	$M_{C^{18}O}(R < 90 \text{ au}) (M_{\odot})$	$M_{\text{gas}}(R < 90 \text{ au}) (M_{\odot})$	$M_{\text{dust}}(R < 90 \text{ au}) (M_{\odot})$	g/d	α_{turb}	$\alpha_{\text{visc}}(R < 90 \text{ au})$
A_{min}	1.7×10^{-6}	1.9×10^{-8}	7.9×10^{-4}	5.0×10^{-4}	2	6.3×10^{-3}	1.2
A_{max}	1.4×10^{-7}	1.9×10^{-8}	9.6×10^{-3}	5.0×10^{-4}	19	5.3×10^{-4}	0.1
B_{min}	1.7×10^{-6}	2.1×10^{-8}	8.7×10^{-4}	1.3×10^{-4}	7	2.7×10^{-3}	1.1
B_{max}	1.4×10^{-7}	2.1×10^{-8}	1.1×10^{-2}	1.3×10^{-4}	82	2.2×10^{-4}	0.1
C_{min}	1.7×10^{-6}	1.9×10^{-8}	7.6×10^{-4}	1.3×10^{-4}	6	1.7×10^{-3}	1.2
C_{max}	1.4×10^{-7}	1.9×10^{-8}	9.3×10^{-3}	1.3×10^{-4}	71	1.4×10^{-4}	0.1
D_{min}	1.7×10^{-6}	1.6×10^{-8}	6.6×10^{-4}	1.6×10^{-4}	4	2.6×10^{-4}	1.4
D_{max}	1.4×10^{-7}	1.6×10^{-8}	8.0×10^{-3}	1.6×10^{-4}	50	2.1×10^{-5}	0.1
E_{min}	1.7×10^{-6}	2.7×10^{-8}	1.2×10^{-3}	3.1×10^{-4}	4	2.5×10^{-4}	0.8
E_{max}	1.4×10^{-7}	2.7×10^{-8}	1.4×10^{-2}	3.1×10^{-4}	45	2.0×10^{-5}	0.1

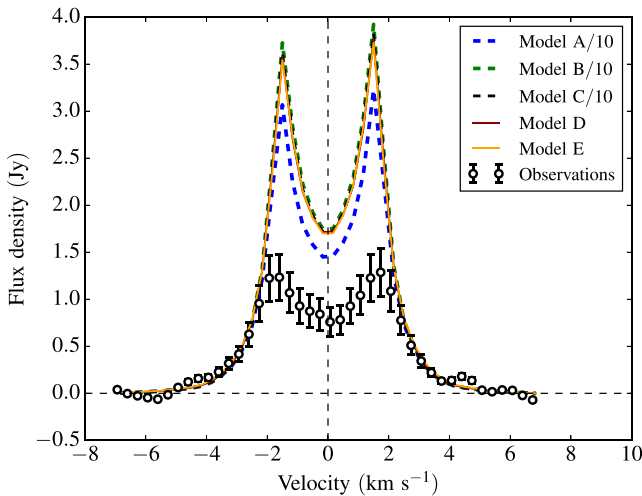


Figure 8. $C^{18}O$ line profile for the whole disc for our five fiducial models (colours) and as observed (dots, error bars represent a 10 per cent flux calibrations uncertainty; Guidi et al. 2016). The profiles were centred around a velocity of 0 km s^{-1} . All models from the same series (that have $C^{18}O$ abundances in the allowed range) have the same line profile (as they have different $C^{18}O$ abundances and gas masses, but the same $C^{18}O$ mass). Our models match the emission from the inner disc regions (wings of the line profile) very well, whereas they overpredict the emission in the outer disc regions (peaks of the spectrum). Our modelling approach is, however, best suited for the inner disc regions.

If we add to this the uncertainty in the $C^{18}O$ abundance, we obtain the full range of M_{gas} that can possibly be present in the disc within 90 au based on our calculation of the extreme cases (see Table 7):

$$6.6 \times 10^{-4} M_{\odot} \lesssim M_{\text{gas}}(R < 90 \text{ au}) \lesssim 1.1 \times 10^{-2} M_{\odot}. \quad (13)$$

We plot the $C^{18}O$ surface number density for our five models and three extreme cases as solid colourful lines in Fig. 9 (left y-axis). The $C^{18}O$ surface density profile derived by Qi et al. (2015) falls within the range shown by our models (black dotted line in Fig. 9, extrapolated from 50 au inwards). In Fig. 9, we also give the corresponding H_2 column densities in the same plot (dashed lines, right y-axis), where we have employed the $C^{18}O$ abundances as listed in Table 6.

It is important to note that all eight models yield very similar $C^{18}O$ surface densities. However, due to their different $C^{18}O$ abundances (see Table 6), their corresponding gas masses within 90 au are different by approximately an order of magnitude. Not surprisingly, models B_{max} and C_{max} yield the highest H_2 column densities, given that they have the lowest possible $C^{18}O$ abundance and thus the highest gas mass. Model A_{min} , on the other hand, has the lowest H_2 column density of the models we plot here, as it has the lowest gas mass of all of them. If we were to plot the same for models for $(B-D)_{\text{min}}$, this would be comparable to A_{min} .

Gas-to-dust mass ratios: Here we present an analysis of the average g/d in the inner disc regions. The g/d values for the individual models are given in Table 6 for the fiducial models (A–C)/10, D and E and for the extreme cases in Table 7. It is striking that all models (excluding the extreme cases) have very low g/d values ($9 \lesssim g/d \lesssim 20$). This is significantly lower than the standard value

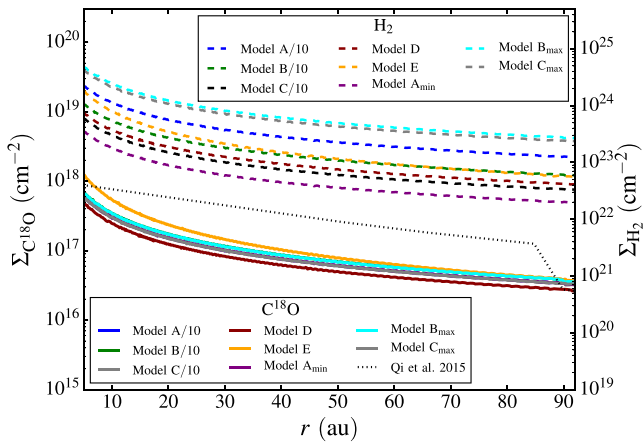


Figure 9. Left y-axis: column number density of $C^{18}O$ for our models (A–C)/10, D, E, A_{\min} , B_{\max} and C_{\max} for regions within the 90 au snowline radius, given by the solid colourful lines. We overplot the one obtained by Qi et al. (2015) (dotted black line, extrapolated from 50 au inwards). Right y-axis: corresponding column density of H_2 , given by the dashed lines for the individual models. The masses of both $C^{18}O$ and H_2 that correspond to these column densities are given in Table 6.

of 100 as observed in the ISM. However, models B_{\max} and C_{\max} do – by construction – have more ISM-like g/d values (~ 80 and ~ 70 , respectively). These are the maximum g/d values (and thus the maximum M_{gas} (< 90 au)) our models can obtain while still matching the $C^{18}O$ line profiles, as both of these models have the lowest possible fractional abundance of $C^{18}O$ that we consider (see equation 9). We comment more on the possibility of lower $C^{18}O$ abundances below.

It is important to note that similarly we can also obtain models based on A–E – employing the highest possible abundance – that yield the lowest possible g/d while still matching the $C^{18}O$ line profile. These are the cases denoted by ‘min’ in Table 7. For these, the g/d values go to values as low as 2 (A_{\min}).

The low value of $g/d \sim 55$ that Kama, Folsom & Pinilla (2015) infer for the inner disc of HD 163296 using the stellar photosphere is in line with the range of g/d we obtain for the innermost 90 au. On the other hand, this range is significantly lower than the value reported by Williams & Best (2014) ($g/d = 170$). These quantities cannot be compared directly, however, because as we pointed out earlier, our results are derived specifically for the $R < 90$ au region, whereas the modelling by Williams & Best (2014) involves disc emission as a whole and therefore is affected by the assumptions made on the disc vertical structure at large scales inasmuch, as this affects the amount of CO that is frozen out. We also note that the very small contribution of such radii to the SED means that the temperature structure of the outer disc is poorly constrained observationally.

$C^{18}O$ abundance: To estimate the maximum gas mass, we adopt the lowest possible value of the abundance of $C^{18}O$ (as given in equation 9). This corresponds to the lowest CO abundance measured in the ISM (Frerking et al. 1982), combined with the highest isotopic ratio of ^{16}O to ^{18}O of 587 (Wilson 1999). This maximum H_2 mass sets an upper limit to the possible g/d in our models.

In Section 3.1.1, we discussed the direct degeneracy between M_{gas} and α_{turb} in setting the vertical structure of the disc as constrained by the SED. We can see in Table 7 that for some of our models α_{turb} could be decreased further, to be compensated with a proportional

increase in M_{gas} , (e.g. models (A–C) $_{\max}$) if we did not impose a limit on the $C^{18}O$ abundance as discussed above. If indeed the $C^{18}O$ abundance were a free parameter, our models (A–C) would be compatible with an ISM-like g/d of 100. An assumption of the minimum value for the turbulent mixing strength $\alpha = 10^{-4}$ yields a $C^{18}O$ abundance as low as $\sim 2.6 \times 10^{-8}$ (in model series A, corresponding to $g/d \sim 100$). This is lower than the minimum value derived based on the observations of the ISM by a factor of ~ 5 . For models D and E, ISM-like g/d cannot be achieved as we are limited by our lower threshold of α_{turb} as discussed above, and therefore the g/d in these models cannot reach higher values than ~ 10 . We can conclude that $g/d = 100$ is possible if one is prepared to assume lower $C^{18}O$ abundances. However, this is only true for model series A–C which are the least plausible of our models because their a_{\min} values of 0.5–0.8 μm are only marginally consistent with the result of Garufi et al. (2014), where the scattered light observations of HD 163296 imply that the disc surface is dominated by sub-micron-sized grains.

A mechanism to decrease the CO (and isotopologue) abundances, and thus permit a more ISM-like g/d , is described in Reboussin et al. (2015). Through this mechanism, the C atoms generated through CO photodissociation in the upper layers are effectively removed through formation of species other than CO (e.g. CO_2 and CH_4). Photodissociation is normally localized in the disc surface, and the $C^{18}O$ abundance may be affected only if the CO dissociating photons were able to penetrate to the mid-plane, or if the surface continued to be depleted of CO over very long time-scales. Thus far, comparison of the CO (and isotopologue) abundance to the H_2 density has only been possible for one, particularly old disc, TW Hya (Favre et al. 2013; Schwarz et al. 2016). These works measure the abundance of CO and its isotopologues to be about 100 times lower than their ISM values.

Dust dynamics: The outer regions of the disc are known to be deficient in sub-mm grains (as deduced from the outer radius in the sub-mm continuum compared with that in CO; see also Guidi et al. 2016). Such concentration of sub-mm dust in the inner disc can be explained in terms of drag-mediated migration of solids. We have used the mid-plane density and temperature profiles of our favoured models to estimate the Stokes number (ratio of drag time-scale to dynamical time-scale) as a function of grain size. We find a Stokes number of close to unity (which corresponds to maximal radial migration) for mm-sized grains in the region of the CO snowline.

The majority of our models have g/d ratios that are considerably below the ISM ratio of 100. Indeed, we can only approach this value if we assume a very low fractional abundance of $C^{18}O$ and assume a grain population that is highly depleted in sub-micron grains (this latter is required in order not to overpredict the infrared flux, given the relatively high temperatures obtained in the case of dust supported in gas-rich discs). However, Garufi et al. (2014) find from their studies of scattered light that there are sub-micron-sized particles present in the inner disc regions, thus the $a_{\min} = 0.8$ and 0.5 μm in models B_{\max} and C_{\max} are only marginally consistent with this requirement. We conclude that the available data require significant deviation from primordial conditions, either in terms of depletion of gas or else in terms of depletion of small grains.

Mid-plane gas-to-dust ratios: It is important to note that the g/d values we have presented so far are average values. Focusing on the ratio of the gas-to-dust density in the inner disc mid-plane now, we show a plot of their ratio in Fig. 10. All our models show very low ratios of $\rho_{\text{gas}}/\rho_{\text{dust}}$ in the mid-plane (between ~ 0.01 and 20) within

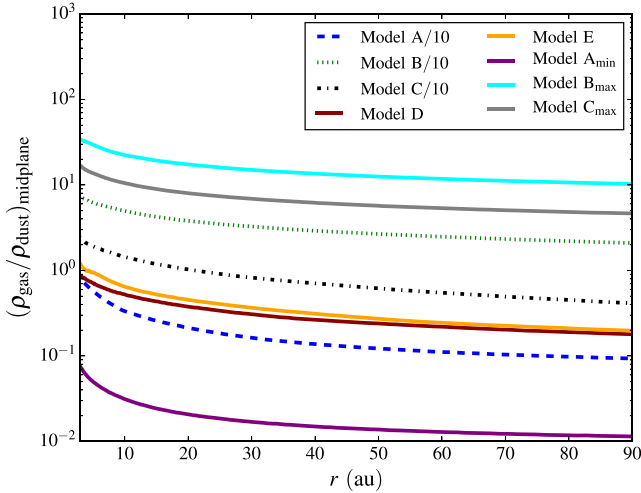


Figure 10. Gas-to-dust mass ratio in the disc mid-plane for our models (A–C)/10, D, E, A_{min}, B_{max} and C_{max} in the inner disc regions ($R < 90$ au).

a radius of 90 au. It is interesting to mention that model B/10, B_{max} and C_{max} have the highest ratio (around ~ 10). Model A_{min} has a g/d of as low as ~ 0.01 , which is not surprising given that its average g/d ratio is ~ 2 and thus the lowest possible in all our models. The fact that $\rho_{\text{gas}}/\rho_{\text{dust}}$ in the mid-plane is lower than the average g/d as discussed above is a result of the dust settling in our models.

Viscosity: Using the masses of H₂ within a radius of 90 au (Table 6), we calculate the viscosity parameter α_{visc} of the inner disc regions. The mass accretion rate of HD 163296 is measured to be within the range $(0.8\text{--}4.5) \times 10^{-7} M_{\odot} \text{ yr}^{-1}$ (Garcia Lopez et al. 2015). The viscosity parameter is given by

$$\alpha_{\text{visc}} = \left(\frac{H}{r} \right)^{-2} \frac{\tau_{\text{dyn}}}{\tau_{\text{visc}}}. \quad (14)$$

The dynamical time-scale of our models at 90 au is

$$\tau_{\text{dyn}}(90 \text{ au}) = \Omega_{\text{k}}^{-1} \sim 100 \text{ yr}. \quad (15)$$

The time-scale of the flow can be obtained by

$$\tau_{\text{flow}}(90 \text{ au}) = \frac{M_{\text{gas}}(90 \text{ au})}{\dot{M}}, \quad (16)$$

which will thus vary depending on the masses of H₂ within 90 au as given in Table 6. The scaleheight of our models is $H/r \sim 0.1$. Equating τ_{visc} and τ_{flow} , we obtain from equation (14) a range of α_{visc} of

$$0.2 \times \left(\frac{\dot{M}}{10^{-7} M_{\odot} \text{ yr}^{-1}} \right) < \alpha_{\text{visc}} < 0.7 \times \left(\frac{\dot{M}}{10^{-7} M_{\odot} \text{ yr}^{-1}} \right), \quad (17)$$

as given in detail for the respective models in Table 6. When considering the models with minimum and maximum M_{gas} (Table 7), the range of α_{visc} we obtain is between 0.1 and 1.4. The values we obtain for α_{visc} are much higher than those found in magnetohydrodynamical simulations of the outer regions of discs in T Tauri stars (Simon et al. 2013a), suggesting that more efficient angular momentum transport (such as that linked to a large-scale net magnetic field and associated wind; Simon et al. 2013b) may be required. We also note that our derived α_{visc} values are around two orders

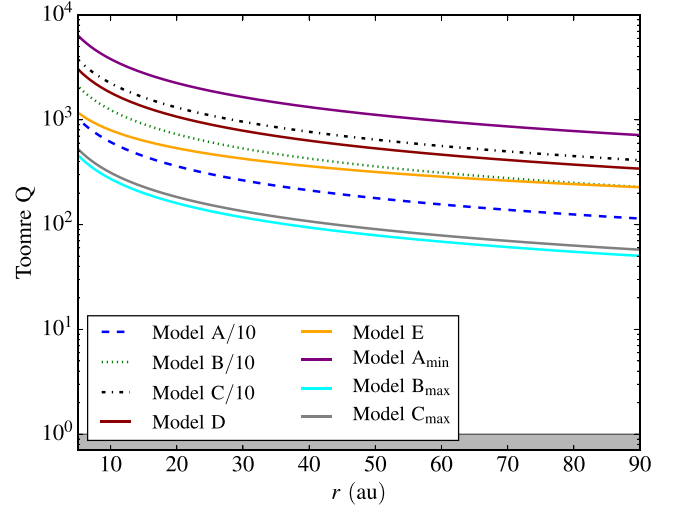


Figure 11. Range of Toomre Q parameter for our models (A–C)/10, D, E, A_{min}, B_{max} and C_{max} which we had found to match the observed SED, the snowline radius and the C¹⁸O emission within 90 au. The region where $Q < 1$ (and the disc potentially gravitationally unstable) is shaded in grey. We find that none of our models reaches this critical regime and all are well above the threshold.

of magnitude greater than the maximum values of α_{turb} allowed by our modelling. This suggests that the efficient transport of angular momentum in this disc is not accompanied by the vigorous level of vertical motions that would be expected in the case of a turbulent viscosity model.

Gravitational instability: We can estimate the gravitational stability of HD 169392 by evaluating the Toomre stability parameter

$$Q = \frac{c_s \Omega}{\pi \Sigma G} < 1 \quad (18)$$

in our models, where c_s is the sound speed, Ω the Keplerian frequency and Σ the disc surface density (Toomre 1964) and where self-gravity becomes important at a Q value of close to unity. We thus study the mid-plane Q parameter as a function of radius in all our eight disc models ((A–C)/10, D, E, A_{min}, B_{max} and C_{max}) and plot the results in Fig. 11.

We find that all of our models are well above the threshold value of $Q = 1$. This implies that none of the models are close to being gravitationally unstable at radii < 90 au; we, however, caution that we cannot assess this quantity in the outer disc, given the sensitivity to the degree of freeze-out in these outer disc regions.

5 CONCLUSIONS

We combine SED fitting, the location of the CO snowline and spatially resolved C¹⁸O line emission to help resolve degeneracies in the determination of protoplanetary disc properties, using the example of HD 163296, of which we estimate the properties. We draw the following main conclusions from this work.

(i) Any one of the aforementioned diagnostics is on its own insufficient to robustly determine the disc properties; however, we demonstrate that together they become much more powerful tools. SED and CO snowline fitting alone could result in a disc mass almost an order of magnitude higher than the mass obtained when C¹⁸O observations are included.

(ii) The observed $C^{18}O$ line flux, together with SED and CO snowline modelling, unambiguously indicates the mass of gas-phase $C^{18}O$ within the 90 au snowline radius, $M_{C^{18}O}(R < 90 \text{ au}) \approx (2-3) \times 10^{-8} M_{\odot}$. We obtain a total gas mass $M_{\text{gas}}(R < 90 \text{ au}) \approx (0.7-11) \times 10^{-3} M_{\odot}$ within the snowline radius, taking into account the uncertainties in the fractional abundance of $C^{18}O$.

(iii) Our modelling approach is best suited for the inner disc regions (within the snowline radius). The emission from the outer disc regions is crucially dependent on the vertical temperature structure and the location of the CO ice surface, so we do not aim to match these. From this, we can conclude that it is important to constrain the vertical temperature of the disc well through physically consistent SED models for the inner disc (as we presented here) and combine these with, for example, high-resolution imaging of multiple CO isotopes in the outer disc (see e.g. Qi et al. 2015).

(iv) For the range of α_{turb} from $(0.1-6.3) \times 10^{-3}$, most of our models of HD 163296 imply gas-to-dust mass ratios in the range $g/d = 10-20$, significantly lower than the ISM value of 100. If we are prepared to also consider models with minimum dust grain sizes of $\sim 0.5 \mu\text{m}$ that are not fully consistent with scattered light observations (Garufi et al. 2014) that also have very low (high) fractional abundance of $C^{18}O$, models with g/d as large as 80 (as small as 2) also match the observations. On top of this and only for these extreme models, $g/d = 100$ may be achieved if the CO abundance is anomalous due to e.g. C-sequestration.

(v) We obtain a high $\alpha_{\text{visc}} \sim 0.2-0.7$ for our models of the inner disc regions, or even up to values of $\alpha_{\text{visc}} \sim 1.4$ (0.1), if we allow for $C^{18}O$ to be very over(under)abundant with respect to the ISM abundances. The notably high ratio of α_{visc} to α_{turb} provides evidence against a turbulent model for angular momentum transport in this disc.

(vi) From analysis of the temperature and density profiles obtained from our models, we find that the disc is not likely to be susceptible to gravitational instability.

The approach to interpretation outlined in this paper will allow us to maximize the value of existing and future high-quality observations with ALMA. This work stresses the importance of $C^{18}O$ observations especially for the warm Herbig Ae discs, which are the prime targets for the application of the methods outlined in this paper.

ACKNOWLEDGEMENTS

We would like to thank the anonymous reviewer for their thorough report and suggestions that have improved the work. This paper makes use of the following ALMA data: ADS/JAO.ALMA#2011.0.00010.SV. ALMA is a partnership of ESO (representing its member states), NSF (USA), and NINS (Japan), together with NRC (Canada) and NSC and ASIAA (Taiwan), in cooperation with the Republic of Chile. The Joint ALMA Observatory is operated by ESO, AUI/NRAO and NAOJ.

This work has been supported by the DISCSIM project, grant agreement 341137 funded by the European Research Council under ERC-2013-ADG. DMB is funded by this ERC grant and an STFC studentship. OP is supported by the Royal Society Dorothy Hodgkin Fellowship. During a part of this project, OP was supported by the European Union through ERC grant number 279973. TJH is funded by the STFC consolidated grant ST/K000985/1. We thank the DISCSIM group at the IoA Cambridge and especially Richard Booth and Attila Juhász for helpful discussions.

REFERENCES

- Acke B., Min M., van den Ancker M. E., Bouwman J., Ochsendorf B., Juhasz A., Waters L. B. F. M., 2009, *A&A*, 502, L17
- Aikawa Y., Nomura H., 2006, *ApJ*, 642, 1152
- Akiyama E., Momose M., Kitamura Y., Tsukagoshi T., Shimada S., Koyama S., Hayashi M., 2013, *PASJ*, 65, 123
- Andrews S. M., Williams J. P., 2007, *ApJ*, 659, 705
- Andrews S. M., Wilner D. J., Hughes A. M., Qi C., Dullemond C. P., 2009, *ApJ*, 700, 1502
- Andrews S. M., Wilner D. J., Hughes A. M., Qi C., Dullemond C. P., 2010, *ApJ*, 723, 1241
- Beckwith S., Sargent A., 1987, in Appenzeller I., Jordan C., eds, *Proc. IAU Symp. 122, Circumstellar Matter*. Kluwer, Dordrecht, p. 81
- Beckwith S. V. W., Sargent A. I., Chini R. S., Guesten R., 1990, *AJ*, 99, 924
- Berrilli F., Corciulo G., Ingrassio G., Lorenzetti D., Nisini B., Strafella F., 1992, *ApJ*, 398, 254
- Boley A. C., Durisen R. H., 2010, *ApJ*, 724, 618
- Boss A. P., Yorke H. W., 1996, *ApJ*, 469, 366
- Bouwman J., de Koter A., van den Ancker M. E., Waters L. B. F. M., 2000, *A&A*, 360, 213
- Clayton G. C., Wolff M. J., Sofia U. J., Gordon K. D., Misselt K. A., 2003, *ApJ*, 588, 871
- Collings M. P., Anderson M. A., Chen R., Dever J. W., Viti S., Williams D. A., McCoustra M. R. S., 2004, *MNRAS*, 354, 1133
- Dartois E., Dutrey A., Guilloteau S., 2003, *A&A*, 399, 773
- de Gregorio-Monsalvo I. et al., 2013, *A&A*, 557, A133
- Draine B. T., 2006, *ApJ*, 636, 1114
- Dullemond C. P., 2002, *A&A*, 395, 853
- Dutrey A., Guilloteau S., Simon M., 1994, *A&A*, 286, 149
- Dutrey A., Guilloteau S., Duvert G., Prato L., Simon M., Schuster K., Menard F., 1996, *A&A*, 309, 493
- Favre C., Cleeves L. I., Bergin E. A., Qi C., Blake G. A., 2013, *ApJ*, 776, L38
- Flaherty K. M., Hughes A. M., Rosenfeld K. A., Andrews S. M., Chiang E., Simon J. B., Kerzner S., Wilner D. J., 2015, *ApJ*, 813, 99
- Forgan D., Rice K., 2013, *MNRAS*, 432, 3168
- Fray N., Schmitt B., 2009, *Planet. Space Sci.*, 57, 2053
- Frerking M. A., Langer W. D., Wilson R. W., 1982, *ApJ*, 262, 590
- Garcia Lopez R., Tambovtseva L. V., Schertl D., Grinin V. P., Hofmann K.-H., Weigelt G., Caratti o Garatti A., 2015, *A&A*, 576, A84
- Garrod R. T., Pauly T., 2011, *ApJ*, 735, 15
- Garufi A., Quanz S. P., Schmid H. M., Avenhaus H., Buenzli E., Wolf S., 2014, *A&A*, 568, A40
- Grady C. A. et al., 2000, *ApJ*, 544, 895
- Guidi G. et al., 2016, *A&A*, 588, A112
- Harries T. J., 2000, *MNRAS*, 315, 722
- Haworth T. J., Harries T. J., 2012, *MNRAS*, 420, 562
- Hersant F., Wakelam V., Dutrey A., Guilloteau S., Herbst E., 2009, *A&A*, 493, L49
- Isella A., Testi L., Natta A., Neri R., Wilner D., Qi C., 2007, *A&A*, 469, 213
- Isella A., Carpenter J. M., Sargent A. I., 2009, *ApJ*, 701, 260
- Jørgensen J. K., Visser R., Williams J. P., Bergin E. A., 2015, *A&A*, 579, A23
- Kama M., Folsom C. P., Pinilla P., 2015, *A&A*, 582, L10
- Lacy J. H., Knacke R., Geballe T. R., Tokunaga A. T., 1994, *ApJ*, 428, L69
- McMullin J. P., Waters B., Schiebel D., Young W., Golap K., 2007, in Shaw R. A., Hill F., Bell D. J., eds, *ASP Conf. Ser. Vol. 376, Astronomical Data Analysis Software and Systems XVI*. Astron. Soc. Pac., San Francisco, p. 127
- Mannings V., Sargent A. I., 1997, *ApJ*, 490, 792
- Mathews G. S. et al., 2013, *A&A*, 557, A132
- Mathis J. S., Rumpl W., Nordsieck K. H., 1977, *ApJ*, 217, 425
- Meeus G. et al., 2010, *A&A*, 518, L124
- Meijer J., Dominik C., de Koter A., Dullemond C. P., van Boekel R., Waters L. B. F. M., 2008, *A&A*, 492, 451
- Mendigutia I., Mora A., Montesinos B., Eiroa C., Meeus G., Merín B., Oudmijer R. D., 2012, *A&A*, 543, A59

- Min M., Dullemond C. P., Dominik C., de Koter A., Hovenier J. W., 2009, *A&A*, 497, 155
- Miotello A., Bruderer S., van Dishoeck E. F., 2014, *A&A*, 572, A96
- Mulders G. D., Dominik C., 2012, *A&A*, 539, A9
- Natta A., Testi L., Neri R., Shepherd D. S., Wilner D. J., 2004, *A&A*, 416, 179
- Panić O., Hogerheijde M. R., Wilner D., Qi C., 2008, *A&A*, 491, 219
- Panić O., Ratzka T., Mulders G. D., Dominik C., van Boekel R., Henning T., Jaffe W., Min M., 2014, *A&A*, 562, A101
- Perez S. et al., 2015, *ApJ*, 798, 85
- Qi C., D'Alessio P., Öberg K. I., Wilner D. J., Hughes A. M., Andrews S. M., Ayala S., 2011, *ApJ*, 740, 84
- Qi C. et al., 2013a, *Science*, 341, 630
- Qi C., Öberg K. I., Wilner D. J., 2013b, *ApJ*, 765, 34
- Qi C., Öberg K. I., Andrews S. M., Wilner D. J., Bergin E. A., Hughes A. M., Hogerheijde M., D'Alessio P., 2015, *ApJ*, 813, 128
- Reboussin L., Wakelam V., Guilloteau S., Hersant F., Dutrey A., 2015, *A&A*, 579, A82
- Rosenfeld K. A., Andrews S. M., Hughes A. M., Wilner D. J., Qi C., 2013, *ApJ*, 774, 16
- Rundle D., Harries T. J., Acreman D. M., Bate M. R., 2010, *MNRAS*, 407, 986
- Schwarz K. R., Bergin E. A., Cleeves L. I., Blake G. A., Zhang K., Öberg K. I., van Dishoeck E. F., Qi C., 2016, *ApJ*, 823, 91
- Semenov D., Pavlyuchenkov Y., Schreyer K., Henning T., Dullemond C., Bacmann A., 2005, *ApJ*, 621, 853
- Simon J. B., Bai X.-N., Stone J. M., Armitage P. J., Beckwith K., 2013a, *ApJ*, 764, 66
- Simon J. B., Bai X.-N., Armitage P. J., Stone J. M., Beckwith K., 2013b, *ApJ*, 775, 73
- Simon J. B., Hughes A. M., Flaherty K. M., Bai X.-N., Armitage P. J., 2015, *ApJ*, 808, 180
- Thi W. F. et al., 2013, *A&A*, 557, A111
- Thi W.-F. et al., 2014, *A&A*, 561, A50
- Tilling I. et al., 2012, *A&A*, 538, A20
- Toomre A., 1964, *ApJ*, 139, 1217
- van den Ancker M. E., de Winter D., Tjin A Djie H. R. E., 1998, *A&A*, 330, 145
- van Zadelhoff G.-J., van Dishoeck E. F., Thi W.-F., Blake G. A., 2001, *A&A*, 377, 566
- Visser R., van Dishoeck E. F., Black J. H., 2009, *A&A*, 503, 323
- Williams J. P., Best W. M. J., 2014, *ApJ*, 788, 59
- Wilson T. L., 1999, *Rep. Prog. Phys.*, 62, 143
- Woitke P. et al., 2016, *A&A*, 586, A103
- Wright C. M. et al., 2015, *MNRAS*, 453, 414
- Youdin A. N., Lithwick Y., 2007, *Icarus*, 192, 588

This paper has been typeset from a $\text{\TeX}/\text{\LaTeX}$ file prepared by the author.